

Defect Spectroscopy on  
Cu(In,Ga)(S,Se)<sub>2</sub>-Based  
Heterojunction Solar Cells:  
Role of the Damp-Heat Treatment

Dem Fachbereich Physik der  
Carl von Ossietzky Universität Oldenburg  
zur Erlangung des Grades eines  
**Doktors der Naturwissenschaften**  
(Dr. rer. nat.)  
vorgelegte Dissertation.

Carsten Deibel

geboren am 11. Februar 1975  
in Wuppertal

Erstgutachter: Prof. Dr. Jürgen Parisi  
Zweitgutachter: Priv.-Doz. Dr. Vladimir Dyakonov

Tag der Disputation: 17. Dezember 2002

## Abstract

The changes of defect characteristics induced by accelerated lifetime tests on solar cells of the heterostructure  $\text{ZnO/CdS/Cu(In,Ga)(S,Se)}_2/\text{Mo}$  are investigated. Encapsulated modules were shown to be stable against water vapor and oxygen under outdoor conditions, whereas the fill factor and open-circuit voltage of non-encapsulated test cells are reduced after prolonged damp-heat treatment in the laboratory, leading to a reduced energy conversion efficiency. We subject non-encapsulated test cells to extended damp-heat exposure at  $85^\circ\text{C}$  ambient temperature and 85% relative humidity for various time periods (6h, 24h, 144h, 294h, and 438h). In order to understand the origin of the pronounced changes of the cells, we apply temperature-dependent capacitance–voltage measurements, admittance spectroscopy, and deep-level transient spectroscopy. We observe the presence of electronic defect states which showed an increasing activation energy due to damp-heat exposure. The corresponding attempt-to-escape frequency and activation energy of these defect states obey the Meyer-Neldel relation. We conclude that the response originates from an energetically continuous distribution of defect states in the vicinity of the CdS/chalcopyrite interface. The increase in activation energy indicates a reduced band bending at the  $\text{Cu(In,Ga)(S,Se)}_2$  surface. We observe changes in the bulk defect spectra due to the damp-heat treatment as well.

## Kurzfassung

Die Untersuchung der geänderten Defektcharakteristika, die durch beschleunigte Lebensdauertests von  $\text{ZnO/CdS/Cu(In,Ga)(S,Se)}_2/\text{Mo}$  Dünnschichtsolarzellen verursacht werden, sind Ziel dieser Arbeit. Gekapselte Module sind stabil gegenüber Wasserdampf und Sauerstoff, der Füllfaktor und die Leerlaufspannung von ungekapselten Testzellen hingegen werden durch eine künstliche Alterung im Labor verringert; dies führt zu einer verminderten Energieumwandlungseffizienz. Diese künstliche Alterung wird anhand des ‘Damp-Heat’ Tests durchgeführt, bei dem die ungekapselten Zellen feucht-warmer Luft von  $85^\circ\text{C}$  Umgebungstemperatur und 85% relativer Luftfeuchtigkeit für verschiedene Zeitdauern (6h, 24h, 144h, 294h und 438h) ausgesetzt. Um den Ursprung der geänderten Solarzellenparameter näher zu beleuchten, wenden wir temperaturabhängige Kapazitäts-Spannungsmessungen, Admittanzspektroskopie und Transiente Störstellenspektroskopie an. Wir beobachten elektronische Defektzustände, welche eine proportional zur Dauer der ‘Damp-Heat’ Belastung erhöhte Aktivierungsenergie aufweisen. Die korrespondierende Fluchtfrequenz (der Vorfaktor der Emissionsrate) und die Aktivierungsenergie dieser Defektzustände folgen der Meyer-Neldel Regel. Wir folgern, daß eine kontinuierliche Energieverteilung von Defektzuständen in der Nähe der  $\text{CdS/Cu(In,Ga)(S,Se)}_2$  Grenzfläche dafür verantwortlich gemacht werden kann. Die erhöhte Aktivierungsenergie deutet demnach auf eine Verminderung der Bandverbiegung an der  $\text{Cu(In,Ga)(S,Se)}_2$  Oberfläche hin. Zudem beobachten wir durch die ‘Damp-Heat’ Belastung induzierte Änderungen in den Defektspektren von Volumenstörstellen.



# Contents

<b>1</b>	<b>Introduction</b>	<b>1</b>
<b>2</b>	<b>Cu(In,Ga)(S,Se)<sub>2</sub>-Based Solar Cells</b>	<b>3</b>
2.1	Structure . . . . .	3
2.1.1	Front Contact . . . . .	3
2.1.2	Buffer Layer . . . . .	4
2.1.3	Absorber Layer . . . . .	4
2.1.4	Back Contact . . . . .	6
2.2	Investigated Samples . . . . .	6
<b>3</b>	<b>Defect States and Experimental Methods</b>	<b>7</b>
3.1	Defect States . . . . .	7
3.1.1	Carrier Recombination Kinetics . . . . .	7
3.1.2	Effects Influencing the Emission Rate . . . . .	9
3.2	Defect Spectroscopy . . . . .	11
3.2.1	Admittance Spectroscopy . . . . .	11
3.2.2	Deep-Level Transient Spectroscopy . . . . .	13
3.2.3	Capacitance–Voltage Measurement . . . . .	17
3.3	Experimental Equipment . . . . .	18
<b>4</b>	<b>Experimental Results</b>	<b>21</b>
4.1	General Observations . . . . .	21
4.2	Interface Defect States . . . . .	22
4.2.1	Interface Defect State $\beta$ . . . . .	22
4.2.2	Interface Defect State $\theta$ . . . . .	26
4.3	Bulk Defects . . . . .	27
4.3.1	Recombination Center $\epsilon$ . . . . .	27
4.3.2	Acceptor-like Defect State $\gamma$ . . . . .	29
4.3.3	Acceptor-like Defect State $\zeta$ . . . . .	29
4.3.4	Defect State $\kappa$ . . . . .	30
4.3.5	Defect State $\eta$ . . . . .	31
<b>5</b>	<b>Numerical Simulations</b>	<b>33</b>
5.1	On the Validity of the Open-Circuit Voltage Extrapolation Method . . . . .	33
5.2	Damp-Heat Treatment of Cu(In,Ga)(S,Se) <sub>2</sub> -Based Solar Cells . . . . .	34
<b>6</b>	<b>Discussion</b>	<b>37</b>

---

6.1	Origin of the Defect State $\beta$ . . . . .	37
6.2	Contact Formation . . . . .	40
6.3	On the Influence of the Damp-Heat Treatment . . . . .	41
6.3.1	Window Layer . . . . .	41
6.3.2	Window/Absorber Interface . . . . .	42
6.3.3	Absorber Layer . . . . .	43
6.3.4	Back Contact . . . . .	44
<b>7</b>	<b>Conclusions</b>	<b>47</b>
	<b>Bibliography</b>	<b>51</b>
<b>A</b>	<b>List of Investigated Samples</b>	<b>59</b>
<b>B</b>	<b>List of Symbols</b>	<b>61</b>
<b>C</b>	<b>Parameters and Results of the Numerical Simulations</b>	<b>63</b>

# 1 Introduction

Renewable energies in general and solar cells in particular are becoming an important focus of energy production, especially the prospects of thin film solar cells are of great promise. They offer high energy conversion efficiencies with a relatively low amount of source materials at competitive costs and a favorable energy balance. Thin film solar cells based on the chalcopyrite  $\text{CuInSe}_2$  are closest to commercialization; they have been sold by Siemens Solar (now Shell Solar) since 1998. Considering that this cell concept contains semiconductor layers of mainly polycrystalline nature with more than ten different constituents, it seems surprising that a relatively high performance and reproducibility are achieved. The physical understanding of the underlying principles of electronic transport and morphological properties, however, always remains a step behind the technological invention.

Already in the sixties, the search for direct semiconductors with an appropriate energy gap as absorber of sun light has led to the first  $\text{CdS/CdTe}$  and  $\text{CdS/Cu}_x\text{S}$  solar cells. Unfortunately, these early systems (especially the latter one [1]) showed degradation. In 1975 the use of ternary chalcopyrites as absorber material led to the development of stable single-crystalline thick film  $\text{CdS/CuInSe}_2$  solar cells with energy conversion efficiencies of about 12%, presented by Bell Labs. The first  $\text{CdS/CuInSe}_2$  thin film solar cells were reported by Mickelsen and Chen [2] in 1981 with 9.4% efficiency. The unfavorable absorption edge of  $\text{CdS}$  as window material was addressed in 1988, when Mitchell and Liu [3] presented the heterostructure presently used,  $\text{ZnO/CdS/CuInSe}_2$ , with  $\text{CdS}$  being a thin intermediate layer. This system showed promising performance (energy conversion efficiency of about 14%) and high stability. Today,  $\text{CuInSe}_2$ -based thin film solar cells have achieved relatively high energy conversion efficiencies on laboratory scale devices (18.8% reported in Ref. [4]) as well as large area modules (up to 12.5%) [5, 6, 7], and once again the focus of research and development shifts back from optimizing the performance to achieving a higher (than before) intrinsic stability against environmental hazards. The long-term stability under outdoor conditions for at least 20 years is a key prerequisite for the success of solar cells as a powerful source of renewable energy.

Encapsulated  $\text{Cu(In,Ga)(S,Se)}_2$ -based thin-film modules have been demonstrated to perpetuate their performance over many years under various environmental conditions [8]. In order to understand the potential power losses developing over the course of decades, standardized accelerated lifetime tests assist the investigation to be performed within a few weeks. The acceleration factor of these stress tests relative to a field test is presently still unknown; it would be needed for a reliable extrapolation of the module lifetime based on stress examination results. For that purpose, we look for a better understanding of stress-test induced changes in the device. The most severe part of the well-established IEC 1215 (ISPR) test is an exposure of the cells under investigation to 1000h of damp heat (DH) treatment at a temperature of  $85^\circ\text{C}$  and a relative humidity of 85%. Improved technology and encapsulation

procedures led to reduction of degradation effects, thus, modules fabricated to date passed the accelerated lifetime tests [8, 9]. Non-encapsulated  $\text{Cu}(\text{In,Ga})(\text{S,Se})_2$ -based solar cells, however, showed losses in the fill factor and open-circuit voltage after exposure to the DH test, whereas the short-circuit current remained almost unaffected.

In the present study, I analyze the influence of accelerated lifetime tests on non-encapsulated  $\text{ZnO}/\text{CdS}/\text{Cu}(\text{In,Ga})(\text{S,Se})_2/\text{Mo}$  heterostructure solar cells and  $\text{Cr}/\text{Cu}(\text{In,Ga})(\text{S,Se})_2$  Schottky contacts, focusing on the electronic properties of the  $\text{Cu}(\text{In,Ga})(\text{S,Se})_2$  absorber and the interface between window and absorber. The investigation of defect states applying admittance spectroscopy [10] and deep-level transient spectroscopy [11] (DTLS) allows for monitoring the electronic changes induced by chemical or morphological modifications due to oxygenation and exposure to DH.

The thesis is organized as follows: First, the material system is introduced, with emphasis on the  $\text{Cu}(\text{In,Ga})(\text{S,Se})_2$  absorber (Section 2). In Section 3, the experimental methods used for electrical characterization and the related semiconductor theory are briefly described. The experimental results of current–voltage measurements, admittance spectroscopy, and DLTS concerning the modifications of the electronic properties due to DH exposure are presented in Section 4. One-dimensional simulations of the  $\text{Cu}(\text{In,Ga})(\text{S,Se})_2$  solar cells using the SCAPS package are presented in Section 5. The discussion of the experimental results and the simulations follows in Section 6. Finally, Section 7 gives a summary and the conclusions. The appendix contains lists of the investigated samples (Section A), the mathematical symbols (Section B), and parameters and results of the numerical simulations (Section C).



## 2 Cu(In,Ga)(S,Se)<sub>2</sub>-Based Solar Cells

First of all, the concept of the CuInSe<sub>2</sub>-based solar cells and the function and preparation of each layer will be introduced (Section 2.1), followed by the description of the investigated samples (Section 2.2).

### 2.1 Structure

The n-ZnO/i-ZnO/CdS/Cu(In,Ga)(S,Se)<sub>2</sub>/Mo heterojunctions investigated in our research group are processed by Shell Solar Munich. The schematic structure of this substrate configuration is shown in Figure 2.1. The solar irradiation passes through the transparent and highly conducting n-ZnO window layer and two intermediate layers, the i-ZnO window and the n-CdS buffer. It is finally absorbed in the p-Cu(In,Ga)(S,Se)<sub>2</sub> absorber. The photogenerated holes are transported to the Mo back contact, whereas the electrons are extracted from the ZnO layer. The properties and the preparation of the different layers are explained below.

This overview is kept intentionally brief, as the details necessary for the interpretation of the experimental results are mentioned in the discussion section. More information on CuInSe<sub>2</sub>-based heterojunction solar cells can be found, e.g., in extensive reviews and text books [12, 13].

#### 2.1.1 Front Contact

The task of the front contact of a CuInSe<sub>2</sub>-based solar cell is to let the light be transmitted to the absorber layer and to extract the photogenerated electrons. The transparent conductive oxide ZnO is well-suited for these requirements. The energy bandgap of this semiconductor is about 3.3eV, which corresponds to an absorption edge of about 375nm. Two adjacent layers of ZnO are used in the typical heterostructure: a 800nm thick layer of Al-doped ZnO (n-ZnO), and a 50nm thin i-ZnO layer, the latter being nominally undoped, but intrinsically n-conducting. The former is a degenerated semiconductor and, thus, highly conducting. It is usually deposited using d.c.-sputtering. The i-ZnO layer is radio-frequency (r.f.) sputtered. Earlier, a chemical vapor deposition of the front contact was commonly applied.

In order to learn about the role of the i-ZnO layer in the heterostructure, it has been modelled using a simple two-diode equivalent circuit [14]. Assuming that up to 5% of the polycrystalline absorber layer is very defect rich, the model shows that the performance degrades significantly only in samples without i-ZnO layer. Thus, the i-ZnO layer (together with the buffer layer) provides a small local series resistance to minimize the effect of electronically inferior grains.

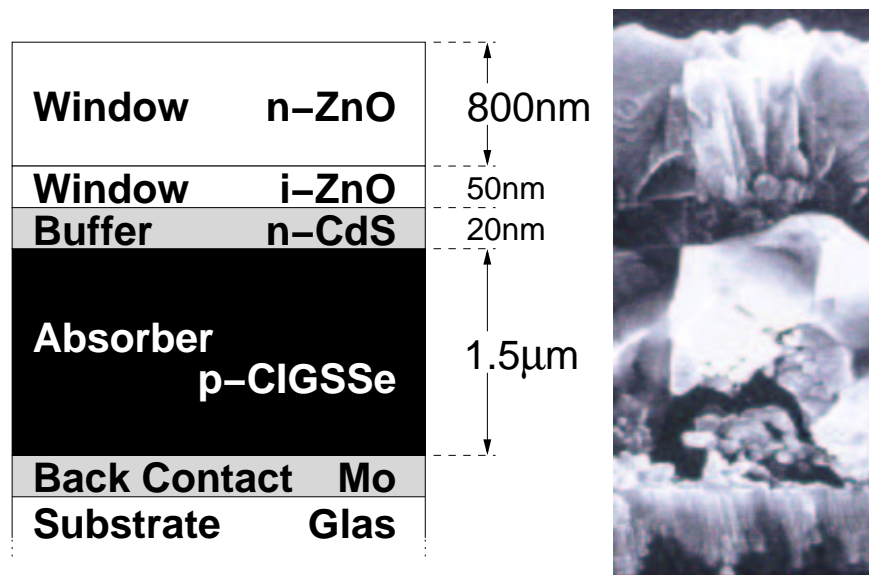


**Figure 2.1:** Cross-sectional structure of Cu(In,Ga)(S,Se)<sub>2</sub>-thin film solar cells. Schematic diagram (left), Scanning-Electron Microscope picture (right).

### 2.1.2 Buffer Layer

Before the ZnO/CdS/Cu(In,Ga)(S,Se)<sub>2</sub> heterojunction has become the common configuration, the binary semiconductor compound CdS served as the front contact [2, 15]. However, as the band gap is only 2.5eV ( $\approx 500\text{nm}$ ) wide, its replacement was an inevitable step for improving the solar cell performance. Nowadays, the thin intermediate CdS layer guarantees the proper contact of window and absorber layers, and is found in all high efficiency CuInSe<sub>2</sub>-based solar cells [4, 16]. However, a search for alternative buffer materials is important in so far as CdS is toxic. Buffer layers like ZnSe [17, 18] or ZnS [19] show very promising results in terms of performance, but are not stable against environmental tests [20], an issue that needs to be addressed.

Rau et al. [12] proposed that the CdS bath deposition undertakes the important role of removing passivating oxygen bonds from the Cu(In,Ga)(S,Se)<sub>2</sub> surface, maintaining the type inversion [21]. Another role of the buffer layer is to protect the absorber layer from sputter damage during the deposition of the front contact.

The transition of the buffer to the absorber layer is non-abrupt, as intermixing of different atomic species takes place [22, 23]. Thus, in contrast to heterojunction systems based on CuInSe<sub>2</sub> single crystals [24], the alignment of the conduction band at the CdS/Cu(In,Ga)(S,Se)<sub>2</sub> interface does not show a significant spike [25]. The part of the buffer layer in light-induced metastable processes has been described and modelled by several groups [26, 27, 28].

### 2.1.3 Absorber Layer

The chalcopyrite CuInSe<sub>2</sub> is a I-III-VI<sub>2</sub>-semiconductor. It can be deposited as a polycrystalline thin film or grown as a single crystal [29], the lattice following the double zincblende structure (Figure 2.2).

As a direct semiconductor,  $\text{CuInSe}_2$  exhibits a high absorption coefficient. The thin films used in modern  $\text{CuInSe}_2$ -based solar cells are polycrystalline and contain Ga and S as additional constituents. The band gap of the resulting quinary  $\text{Cu(In,Ga)(S,Se)}_2$  compound semiconductor can be adjusted over a wide range: from 1.04 eV for pure  $\text{CuInSe}_2$  over 1.4 eV and 1.7 eV for  $\text{CuInS}_2$  and  $\text{CuGaSe}_2$ , respectively, to about 2.4 eV for  $\text{CuGaS}_2$ . The  $\text{Cu(In,Ga)(S,Se)}_2$ -based solar cells processed by Shell Solar show a band gap of 1.1 eV (quantum efficiency measurements), however, at the  $\text{Cu(In,Ga)(S,Se)}_2$  surface the band gap is about 1.4 eV [25], indicating concentration gradients of the different constituents. Virtually no Ga is present at the surface [22], and it is Cu poor [24, 30]. The concentration Ga increases towards the back contact [7]. The S concentration exceeds its stoichiometrical mean value at the front and back interfaces [7].

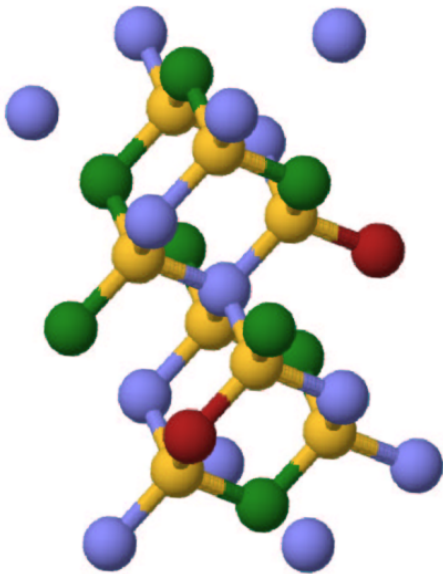


**Figure 2.2:** The double zincblende structure of the chalcopyrite  $\text{Cu(In,Ga)Se}_2$ . Cu (blue), In (green), Ga (red), Se (yellow).

For photovoltaic devices, slightly In-rich  $\text{CuInSe}_2$ -based films are used. The phase diagram [30] illustrates that the material is relatively tolerant against variations of the stoichiometry (especially, if Na and/or Ga are present). However, a Cu-rich composition *during* the film growth is favorable for the growth of large ( $1\ \mu\text{m}$ ) grains, because (in a model by Klenk et al. [31]) a quasi-liquid surface film of  $\text{Cu}_y\text{Se}$  performs the role of a flux agent.  $\text{Cu(In,Ga)(S,Se)}_2$  is not extrinsically doped, but reaches sufficient doping concentrations intrinsically, especially by the shallow acceptor levels due to Cu vacancies [32].

Nearly a decade ago, it was discovered that the unexpected diffusion of Na from the float-glass substrate [33] led to a substantial improvement of the energy conversion efficiency [34, 35]. A controlled incorporation of Na is yielded by a certain amount of a Na-compound deposited on top of the back contact. Na seems to play a similar role as  $\text{Cu}_y\text{Se}$  in so far as a  $\text{Na}_y\text{Se}$  compound is formed, slowing down the grain growth and maintaining the incorporation of Se. Positive effects of Na have been ascribed to the acceptors  $\text{Na}_{\text{In}}$  and  $\text{Na}_{\text{Cu}}$  improving the p-conductivity, the latter possibly preventing the formation of the detrimental donor  $\text{In}_{\text{Cu}}$  [36]. A significant amount of the Na was found to locate at the  $\text{CdS/Cu(In,Ga)Se}_2$  interface [37].

Two routes for preparation of  $\text{CuInSe}_2$ -based thin films are used principally: Coevaporation, in particular the three-stage process [38] used in the currently best laboratory-scale solar cells [4], and the rapid thermal processing (RTP) [5, 39]. As the samples investigated during the course of this thesis are produced by Shell Solar via RTP, this preparation concept is briefly summarized. The absorber layer is formed via a two-step stacked elemental layer process. First, an elemental precursor film is deposited onto the back contact by d.c. magnetron sputtering of alternating layers of CuGa and In and thermal evaporation of Se, the amount of the latter exceeding the stoichiometric requirements by about 40%, in order to compensate for losses during the subsequent formation process. Second, the precursor is heated by tungsten halogen lamps in an RTP furnace with a steep temperature profile, minimizing a dewetting

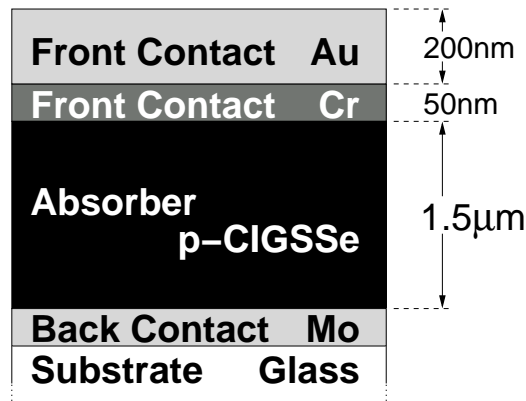


**Figure 2.3:** Schematic cross-sectional view of a Cr/Cu(In,Ga)(S,Se)<sub>2</sub> Schottky contact.

of the Se. This process is performed in a S-containing ambient. The final composition of the absorber layer is monitored to comply with  $\text{Cu}_{0.92}(\text{In}_{0.83}\text{Ga}_{0.17})(\text{S}_{0.18}\text{Se}_{0.82})_2$  using an x-ray fluorescence analyzer system. The maximum temperatures necessary for the absorber formation are well below 600°C.

### 2.1.4 Back Contact

Three layers are deposited onto the soda-lime glass substrates using d.c. magnetron sputtering: a SiN-coating as a barrier for uncontrollable diffusion of Na into the absorber layer, the Mo back contact, and a Na-compound for the controlled incorporation of Na. The Mo/CuInSe<sub>2</sub> transition was proven to be ohmic by performing current–voltage measurements on special structures, which allowed to characterize Mo/CuInSe<sub>2</sub>/Mo and ZnO/CdS/CuInSe<sub>2</sub> junctions simultaneously [40].

## 2.2 Investigated Samples

The investigated samples consist of ZnO/i-ZnO/CdS/Cu(In,Ga)(S,Se)<sub>2</sub>/Mo heterojunction solar cells (see Figure 2.1) and Cr/Cu(In,Ga)(S,Se)<sub>2</sub>/Mo Schottky contacts (see Figure 2.3). An overview of the investigated samples is assembled in Appendix A. The Schottky devices were produced by thermal deposition of a 50nm thick Cr film on top of the uncleaned Cu(In,Ga)(S,Se)<sub>2</sub> surface, followed by a 200nm thick Au layer for mechanical protection [41].

Accelerated lifetime testing of the non-encapsulated samples was performed under the standardized DH conditions at 85°C ambient temperature and 85% relative humidity for various time periods (6h, 24h, 144h, 294h, and 438h). For different sets of samples, the processing sequence was interrupted for a DH treatment after the RTP, the CdS bath deposition, or the i-ZnO sputter procedure, respectively. After 6h or 24h under exposure to heat and humidity, the cell process (or the deposition of the Schottky contact) was continued. Instead of DH treatment, one set of samples was annealed in dry air atmosphere (85°C, 24h) after RTP.

## 3 Defect States and Experimental Methods

The material characteristics of semiconductors are strongly influenced by impurity or defect centers. Some are intentionally incorporated to increase the electric conductivity or control the carrier lifetime (e.g., for high-speed switching applications), but often unwanted impurities or lattice imperfections act as loss factors or lifetime killers (for devices, where a long lifetime is required). In solar cells, high concentrations of defect states diminish the carrier transport capabilities, reducing the energy conversion efficiency. Information on the characteristics of the defect centers can be obtained from the capacitance of Schottky barriers or p–n junctions, using different spectroscopic methods.

First, I would like to establish the basic processes of the interaction of charge carriers with defect states (Section 3.1). The corresponding rate equations are essential for the evaluation of the capacitance spectroscopy measurements (Section 3.2). Finally, the experimental equipment is described briefly in Section 3.3. The books of Blood and Orton [42] and Li [43] provide further details on defect states and their characterization.

### 3.1 Defect States

Defects and impurities can create localized electronic states within the band gap. These bound states are classified as deep or shallow. Historically, a defect state was denoted as shallow if its energy level was close to the conduction band minimum,  $E_C$ , or valence band maximum,  $E_V$ , respectively. Otherwise, it was called a deep level. A more precise definition is used nowadays: A shallow defect state inhibits a long-range Coulomb potential, whereas a defect state with a short-range potential is called a deep level. In order to describe the interaction of defect states with the energy bands, a look at the carrier recombination kinetics is necessary. Physical processes distorting the emission rate will be discussed as well.

#### 3.1.1 Carrier Recombination Kinetics

The carrier recombination kinetics, electronic transitions between (bound) defect states and (free) band states with emission and capture of charge carriers, can be described with theories formulated by Shockley and Read [44], and Hall [45]. Between one defect level and two energy bands, four basic transitions can take place, as indicated in Figure 3.1. The

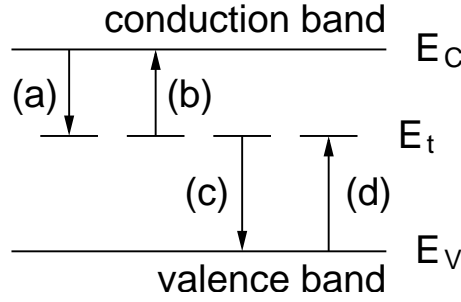


**Figure 3.1:** Four basic electron transitions between defect level  $E_t$  and energy bands. (a) and (b) denote the electron capture and emission, (c) and (d) the hole capture and emission, respectively.

corresponding rate equations are:

$$(a) \quad \text{capture of electrons} = c_n n p_t, \quad (3.1)$$

$$(b) \quad \text{emission of electrons} = e_n n_t, \quad (3.2)$$

$$(c) \quad \text{capture of holes} = c_p p n_t, \quad (3.3)$$

$$(d) \quad \text{emission of holes} = e_p p_t \quad (3.4)$$

with the corresponding capture ( $c_n, c_p$ ) and emission ( $e_n, e_p$ ) rates for electrons and holes, respectively.  $n$  is the concentration of electrons in the conduction band,  $p$  is the concentration of holes in the valence band, and the trapped electron and hole concentrations are  $n_t = N_t f_t$  and  $p_t = N_t(1 - f_t)$ , respectively.  $N_t = n_t + p_t$  is the total trap concentration and  $f_t$  the occupancy probability of electrons in the trap (Fermi-Dirac distribution).

For electron traps, transitions (a) and (b) are dominant. The defect state is a hole trap if (c) and (d) are the main transitions. Recombination centers favor a path along (a) and (c).

Mobile carriers are captured if they come within a certain interaction range of the defect center. The subsequent emission is thermally activated. For electrons, the capture and emission processes can be described as

$$c_n = \sigma_n \bar{v}_n, \quad (3.5)$$

$$e_n = \underbrace{\sigma_n \bar{v}_n N_C}_{\nu_0} \exp\left(-\frac{\Delta E_t}{kT}\right), \quad (3.6)$$

respectively. The capture cross-section  $\sigma_n$  depends on the charge state of the deep level and the charge of the trapped carrier.  $\bar{v}$  denotes the thermal velocity of the charge carriers,  $k$  the Boltzmann factor,  $T$  the absolute temperature, and  $N_C$  the effective density of states of the conduction band. The prefactor  $\nu_0$  is called attempt-to-escape frequency.  $\Delta E_t$  is usually denoted as the activation energy of the defect level. This point of view, however, might be too simplified, as discussed in the next section. Both,  $N_C$  and  $\Delta E_t$  are related to the conduction band for the case of electron emission. The capture and emission rates for holes are expressed in an analogous way.

For determination of the two characteristic parameters of a defect state, the activation energy and the capture cross-section, the temperature dependence of the prefactor of the emission rate has to be considered. The thermal velocity  $\bar{v}_n$  is proportional to  $T^{1/2}$ , whereas

the effective density of states  $N_C \propto T^{3/2}$ . The capture cross-section can be thermally activated as well, which is discussed below.

### 3.1.2 Effects Influencing the Emission Rate

The temperature-dependent emission rates of a certain defect state to the corresponding energy band are a quantity which can be determined experimentally, yielding the trap activation energy and capture cross-section. Therefore, it is necessary to know how these parameters should be interpreted and which effects influence the emission rate. An analysis neglecting these factors cannot account for possible distortions, thus, decreasing the accuracy of the experimentally determined trap characteristics.

The influence of a high concentration of defect states on the emission rate is described in a different part, see Section 3.2.2.

#### Thermodynamics of Carrier Emission

The thermal emission of carriers from a deep state at temperature  $T$  is described by Equation (3.6). The energy  $\Delta E_t$  is usually denoted as the activation energy of the defect state. This point of view, however, turns out to be not quite accurate. Actually, we have  $\Delta E_t \equiv \Delta G$ , the latter being the free energy change for ionization of the state, i.e., the change in the Gibbs free energy  $G$ . Bear in mind that the chemical potential is defined as the increase in Gibbs free energy per electron–hole pair (or carrier-ionized defect pair) at constant temperature and pressure.

$\Delta G$  is defined as

$$\Delta G(T) = \Delta H - T\Delta S \quad (3.7)$$

where  $\Delta H$  is the enthalpy, and  $\Delta S$  the entropy of the process. The temperature-dependent and temperature-independent parts of Equation (3.6) can be separated,

$$e_n(T) = \chi_n \sigma_n(T) \bar{v}_n(T) N_C(T) \exp\left(-\frac{\Delta H}{kT}\right) \quad (3.8)$$

with the entropy factor

$$\chi_n = \exp\left(\frac{\Delta S}{k}\right). \quad (3.9)$$

The problem with the experimental determination of the activation energy of a deep state is that optical measurements are used to determine  $\Delta G$ , but the ‘activation’ energy obtained by electrical measurements usually is the temperature-independent part of  $\Delta G$ ,  $\Delta H$ . Additionally, the ‘apparent’ (i.e., experimentally obtained) capture cross-section deviates from the actual capture cross-section by the entropy factor:

$$\sigma_{n,\text{apparent}} = \chi_n \sigma_n. \quad (3.10)$$

The entropy factor  $\chi_n$  has been reported to be of the order of 10 in some cases [42].

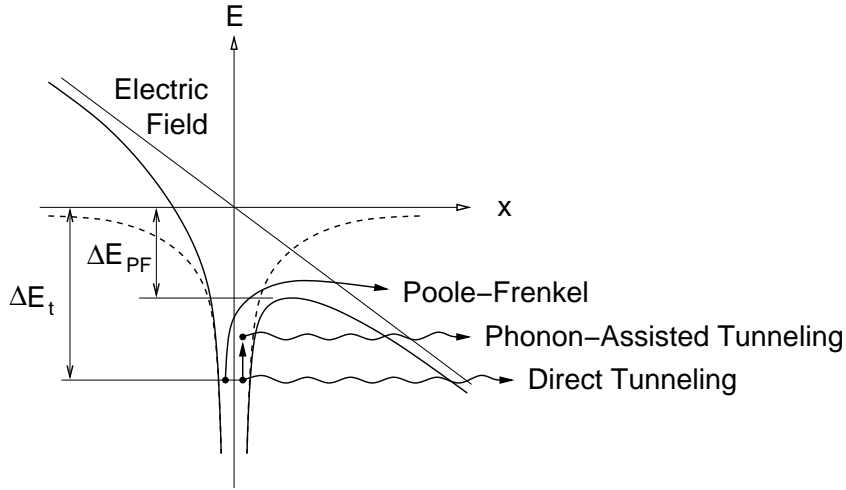


**Figure 3.2:** Position-dependent potential energy  $E(x)$  of a defect state. The potential is distorted by an electric field. The emission of the trapped charge carrier is modified by the Poole-Frenkel effect, direct tunneling, or phonon-assisted tunneling (after Ref. [42]).

### Temperature-Dependent Capture Cross-Section

The capture of charge carriers, Equation (3.5), usually is temperature dependent only due to the thermal velocity of the charges. However, in some materials (e.g., in III-V compounds) a thermally activated capture of charge carriers by a defect state is typical.

The capture process by multiphonon emission [46, 47] follows the relation

$$\sigma_n(T) = \sigma_\infty \exp\left(-\frac{\Delta E_\sigma}{kT}\right), \quad (3.11)$$

where  $\Delta E_\sigma$  is a barrier for carrier capture and  $\sigma_\infty$  a constant prefactor. Other capture mechanisms predict a power-law dependence, e.g.,  $\sigma_n \propto T^{-3}$  for the cascade capture process [42]. The apparent activation energy and capture cross-section are distorted if the temperature behavior of the capture process is unknown.

### Field-Enhanced Emission

The thermal emission rate can be distorted by the junction electric field [47, 48]. Besides a shift of the data points in the Arrhenius representation, it is possible that the emission transient becomes non-exponential due to the spatial variation of the electric field in the depletion region.

The influence of the electric field can affect the emission process in different ways, as illustrated in Figure 3.2. The Poole-Frenkel effect manifests in a reduction of the effective barrier height by  $\Delta E_{PF}$  for thermal emission due to a distortion of the binding energy of the charge carrier to the trap state. The measured activation energy is, thus, lowered by  $\Delta E_{PF}$ . Another possibility is tunneling through this barrier, which can take place directly (for high electric fields of above  $10^7$  V/m) or, more likely, by an effective barrier reduction due to phonons.



## 3.2 Defect Spectroscopy

Defect spectroscopy methods have proven to be important aids in the process of understanding the charge carrier transport in semiconductor heterostructure devices and Schottky contacts. Investigations of defect states allow for monitoring the electronic changes induced by mechanical, chemical or morphological modifications.

The measurement of the junction capacitance of semiconductor devices can be performed in dependence on temperature, bias voltage and frequency of an alternating voltage, in order to gain information on defect states. Admittance spectroscopy (Section 3.2.1) and deep-level transient spectroscopy (Section 3.2.2) help to determine the thermal emission rates of charge carriers from defect states. Capacitance–voltage measurements (Section 3.2.3) are useful in obtaining net doping concentrations.

### 3.2.1 Admittance Spectroscopy

Defect states can be studied by measuring the frequency and temperature dependence of the complex admittance of a junction depletion region. An alternating voltage with the frequency  $f = \omega/2\pi$  is applied to the heterojunction or Schottky contact, modulating the Fermi level. The response to this test signal, the admittance  $Y = G + i\omega C$ , is determined experimentally.  $G$  is the conductance and  $C$  the capacitance. The principle and the power of the admittance spectroscopy will be illustrated on the capacitance. Remarkably, the capacitance of the junction is proportional to the inverse of the space charge width  $W$ ,

$$C = \frac{\epsilon_s}{W}, \quad (3.12)$$

similar to a plate capacitor with plates separated by the distance  $W$ .  $\epsilon_s = \epsilon_r \epsilon_0$  is the dielectric constant of the semiconductor,  $\epsilon_0$  being the permittivity of space and  $\epsilon_r$  the dielectric function of the semiconductor. At low frequencies, transitions of charge carriers from and to defect states respond to the test signal, contributing to the capacitance. At high frequencies, the emission rate of the charge carriers from the defect states (Equation (3.6)) is too low to follow the alternating voltage: these defect states do not contribute to the capacitance any more, and the latter decreases to its geometrical value  $C_{\text{geo}}$ . The frequency  $\omega_0$  where the capacitance step occurs is directly related to the thermal emission rate  $e_n$  of the defect state in question, and the step height is related to the trap concentration. A differentiation of the capacitance step by the frequency,  $-\omega dC/d\omega$ , yields an extremum, allowing one to comfortably obtain emission rate  $e_n$  and step height  $\Delta C$ , as shown in Figure 3.3. The temperature-dependent emission rates can be assembled in an Arrhenius plot ( $\ln e_n/T^2$  versus  $1/T$ ) in order to determine the activation energy and capture cross-section of the defect state, using Equation (3.6).

This experimental method, called admittance spectroscopy, was introduced in the beginning of the seventies by Losee [10, 49]. As the applied alternating voltage is a ‘small signal’, the sample is kept close to thermodynamical equilibrium. Only defect states crossed by the Fermi level can be detected, and no information about the type of the trapped charge carrier is available. The capture cross-section determined by this method is quite inaccurate, as it is obtained by extrapolation.

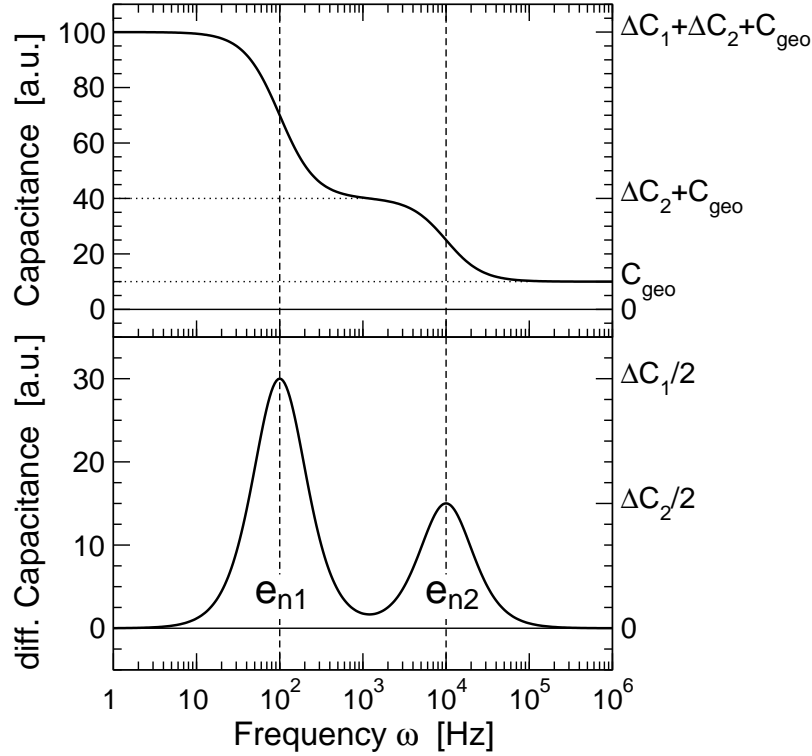


**Figure 3.3:** The calculated capacitance and differentiated (against frequency) capacitance spectra in order to illustrate the operation principle of admittance spectroscopy. Two defect states with different thermal emission rates  $e_{n1}$  and  $e_{n2}$  can be resolved spectroscopically. The capacitance step heights  $\Delta C_1$  and  $\Delta C_2$  can be taken from the differentiated capacitance spectrum.  $C_{\text{geo}}$  is the geometrical capacitance.

Admittance spectroscopy is well-suited for obtaining the frequency dependence of a capacitor (capacitance  $C$ ) connected in parallel to a resistor (resistance  $R = G^{-1}$  (inverse conductance)) in the equivalent circuit diagram. Of course,  $\text{Cu}(\text{In,Ga})(\text{S,Se})_2$ -based devices are represented by a more complex (and unknown) equivalent circuit diagram. However, in this work we assume that a parallel  $R$ - $C$  circuit with an additional series resistance is a sufficient approximation of the real situation. The so-called Nyquist or Cole-Cole plot helps to verify whether or not this equivalent circuit is appropriate for describing a device under study. The real versus the imaginary part of the impedance  $Z$ , being the inverse of the admittance, is plotted. A perfect semi-circle denotes the above mentioned circuit, the diameter signifying the parallel resistance. If this semi-circle is shifted along the  $\text{Re}(Z)$ -axis, an additional series resistance has to be considered; if it is distorted, the influence of an inductance might be responsible.

Admittance spectroscopy can be used to determine defect concentrations. A method derived by Walter et al. [50] can be applied to bulk traps, although several simplifying assumptions have to be made. The concentration of interface defect states can generally be obtained as well. Unfortunately, a very straight forward method derived by Nicollian and

Goetzberger [51] for metal-insulator-semiconductor structures cannot be applied to p–n junctions, in contrast to statements given by Herberholz et al. [52], because in p–n junctions a current across the junction has to be considered [53]. Additionally, two other problems make it difficult to determine the concentration of interface defect states. First, the concentration of an interface defect state can be measured only at the Fermi level. Second, this method works only as long as the Fermi level is not pinned.

### 3.2.2 Deep-Level Transient Spectroscopy

Transient techniques like photocurrent transients have been used to characterize deep traps in semiconductor junctions since the second half of the sixties [54]. Deep-Level Transient Spectroscopy (DLTS) was introduced by Lang [11] in 1974. The principle of this measurement technique can be summarized as follows. A p–n junction or a Schottky contact is perturbed by a voltage or light pulse. After this so-called filling pulse, trapped charge carriers relax back to the steady-state condition. The relaxation time is related to the emission rate of the electrons or holes from the corresponding defect state. Thus, the observation of the emission process as current or capacitance transient allows to obtain characteristic information on the trap level, including concentration and type of trapped charge carrier. The detailed processes of different modes of operation and the evaluation of the transients are discussed in the following sections.

#### Filling Pulses without Minority-Carrier Injection

The principle of a capacitance-DLTS measurement with voltage pulses is illustrated in Figure 3.4. The p<sup>+</sup>–n junction is held at quiescent reverse bias (Figure 3.4(i)). The depletion region has the extension  $W_1$ , the Fermi level intersects the trap state at  $\lambda_1$ . A filling pulse — here without minority-carrier injection, i.e., a maximum voltage of zero volts — diminishes the width of the depletion region to  $W_2$ , the intersection point of the Fermi level with trap state shifts to  $\lambda_2$ . During application of this filling pulse, the trap states located between  $\lambda_1$  and  $\lambda_2$ , shifted below the electron quasi Fermi level capture majority carriers (electrons) as shown in Figure 3.4(ii). After termination of the pulse, the depletion width almost immediately changes back to  $W_1$  due to the short relaxation times of the free charge carriers (order of  $10^{-12}$ s). The trap states, again situated above the electron quasi Fermi-level between  $\lambda_1$  and  $\lambda_2$ , emit the trapped electrons to the conduction band with their characteristic emission rate (Figure 3.4(iii)). The corresponding capacitance of the junction is reduced by trapped majority carriers, because their charge is opposite to that of the net charge of the depletion region on the p-side. Consequently, the capacitance transient  $C(t)$  follows the relation

$$C(t) = C_0 - \Delta C \exp(-e_{nt}), \quad (3.13)$$

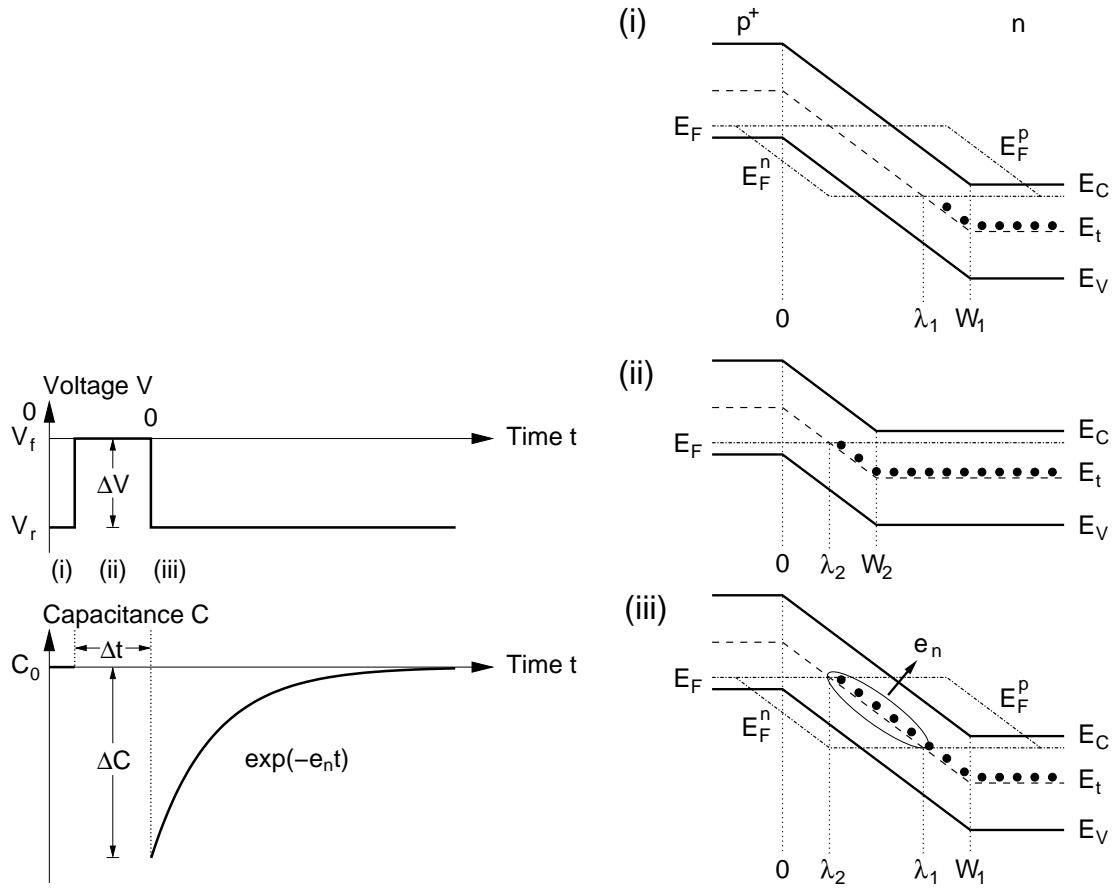


**Figure 3.4:** Principle of a DLTS measurement without minority-carrier injection. Voltage pulse and capacitance transient (left), schematic band diagrams (right). (i)  $p^+-n$  junction containing electron traps under reverse bias  $V_r$  in steady state. (ii) Filling pulse  $V_f$  to zero bias, i.e., without minority-carrier injection. (iii) After the pulse, the filled electron traps are emitted to the conduction band (after Ref. [54]).

where  $C_0$  is the steady-state capacitance at reverse bias, and  $\Delta C$  is the amplitude of the capacitance change, being proportional to the concentration of emitted charge carriers [43]:

$$\begin{aligned} \frac{\Delta C}{C_0} &= -\frac{N_t}{2N_D} \left( 1 - \left( \frac{W_2}{W_1} \right)^2 \right) \left( \frac{e_n}{e_n + e_p} \right) e^{-(e_n + e_p)t} \\ &= \begin{cases} -\frac{N_t}{2N_D} \left( 1 - \left( \frac{W_2}{W_1} \right)^2 \right) e^{-e_n t} & , \text{ if } e_n \gg e_p, \\ 0 & , \text{ if } e_p \gg e_n. \end{cases} \end{aligned} \quad (3.14)$$

Equation (3.14) is valid if several prerequisites are fulfilled. We assume  $\Delta C \ll C_0$ , otherwise the defect concentration is high, and the transients become non-exponential.<sup>1</sup> The defect concentration  $N_t$  and the doping density  $N_D$  have to be uniform. One should bear in mind that several mechanisms exist that distort the emission rates, as described in Section 3.1.2.

<sup>1</sup>The voltage transients observed in constant-capacitance DLTS do not become non-exponential for high defect concentrations. However, such method has not been applied in the present work.

The region between  $W_i$  and  $\lambda_i$  ( $i = 1, 2$ ) is called edge or transition region. The ‘depletion approximation’, used in Equation (3.14) neglects this distinction, i.e., the concentration of free charges in the transition region is defined as zero. In DLTS without minority-carrier injection, only the emission rate of majority charge carriers can be detected.

### Filling Pulses with Minority-Carrier Injection

Under the conditions described in the previous section, the detection of minority-carrier traps is not possible without the injection of minorities (Equation (3.14)).<sup>2</sup> In order to obtain an emission transient of trapped minority carriers, the latter have to be injected by a large forward bias voltage (or light) pulse. After the termination of the injection pulse, capacitance transients due to minority and majority carriers can be detected [43]:

$$\begin{aligned} \frac{\Delta C}{C_0} &= - \left( \frac{N_t}{2N_D} \right) \left( 1 - \left( \frac{W_2}{W_1} \right)^2 \right) \left( \frac{e_n}{e_n + e_p} \right) \left( \eta - \frac{e_p}{e_n} (1 - \eta) \right) e^{-(e_n + e_p)t} \\ &= \begin{cases} - \frac{N_t}{2N_D} \left( 1 - \left( \frac{W_2}{W_1} \right)^2 \right) \eta e^{-e_n t} & , \text{ if } e_n \gg e_p, \\ \frac{N_t}{2N_D} \left( 1 - \left( \frac{W_2}{W_1} \right)^2 \right) (1 - \eta) e^{-e_p t} & , \text{ if } e_p \gg e_n, \end{cases} \end{aligned} \quad (3.15)$$

where

$$\eta = \frac{c_n}{c_n + c_p}. \quad (3.16)$$

The prerequisites for the validity of Equation (3.15) are similar to Equation (3.14). The charge of the trapped carriers is differentiated by the sign of the capacitance transient: Equation (3.13) describes the relaxation of majority carriers. For minority carriers the sign of the relaxation process is changed:

$$C(t) = C_0 + \Delta C \exp(-e_n t). \quad (3.17)$$

### Partial Filling

The Equations (3.14) and (3.15) describing the capacitance transients are applicable for saturating filling pulses. Partial filling, however, can give valuable information on the trap characteristics as well. The capture cross-section determined from the Arrhenius data obtained by DLTS or admittance spectroscopy has been demonstrated to be inaccurate, as it is obtained by extrapolation. A better method is to vary the width of the DLTS filling pulse in subsequent measurements. The amplitude of the capacitance transient  $\Delta C$  increases proportional to the pulse width  $t_f$ , until the defect state becomes saturated (signal  $\Delta C_\infty$ ):

$$\Delta C(t_f) = \Delta C_\infty (1 - \exp(-c_n t_f)). \quad (3.18)$$

The capture rate  $c_n$  inhibits the capture cross-section (Equation (3.5)) and can be determined by plotting  $\ln(\Delta C_\infty - \Delta C(t_f))$  versus  $t_f$ . The capture cross-section obtained is more accurate than the ‘apparent’ capture cross-section determined by standard DLTS measurements.

<sup>2</sup>An exception is discussed in a later section.

### Reverse-DLTS

Reverse-DLTS (R-DLTS) was introduced by Li et al. [55, 56]. In contrast to all other DLTS modes, the process of charge carrier capture is observed. The sample is held at a constant bias, for instance zero bias. During the application of a reverse-bias pulse the traps are emptied, afterwards the transient due to the capture of charge carriers is detected. The sign of the capture transients naturally is opposite to that of the emission transients. The capture process is always faster or, at the intersection of a defect state with the Fermi level, is as fast as the emission. This implies that the R-DLTS signal is due to the capture *at* the intersection point of trap and Fermi level after the termination of the emptying pulse, whereas in a standard DLTS mode the charge carriers are emitted from traps *between*  $\lambda_1$  and  $\lambda_2$  (Figure 3.4). Consequently, a higher spatial resolution can be achieved with R-DLTS.

### Evaluation

In order to analyze the relaxation transients, several methods have been applied. The original setup of Lang [11] used a boxcar averager to detect the maximum change of the exponential decay for two given times, the so-called rate window. This maximum is proportional to the decay rate of the exponential curve. Boxcar averaging requires a full temperature scan for the determination of each data point in the Arrhenius representation ( $\ln e_t/T^2$  versus  $1/T$ ). Another approach was the use of a hardware lock-in amplifier [57], essentially doing the same job as the boxcar averager, but with an improved signal-to-noise ratio and an automatic frequency scan at each temperature. The latter concept is utilized in our Semitrap DLTS spectrometer. Nowadays, the complete transient can be recorded with a high time resolution and can be evaluated using different (software) methods like multi-exponential fit or Laplace transformation. Our new transient-DLTS (based on a Boonton 7200 capacitance bridge) and the methods of evaluation are described in detail in the diploma thesis of Arne Wessel [58].

In the Laplace transformation, a capacitance transient  $C(t) \propto \exp(-e_n t)$  is expanded to a (infinite) series of exponential decays,

$$F(s) = \int_0^{\infty} C(t) e^{-st} dt. \quad (3.19)$$

The transform function is proportional to  $1/(s + e_n)$ , the emission rate  $e_n$  being easily accessible. The software implementation of an improved Laplace transformation method [59] was done by Arne Wessel [58].

### Minority-Carrier Detection without Minority-Carrier Injection

Minority-carrier defect states usually cannot be detected using DLTS without the intentional injection of minority carriers. Optical injection is the common practice for Schottky contacts. In case of the heterojunctions, injection voltage pulses can be applied. However, for Schottky junctions based on n-Si, the observation of minority-carrier traps with DLTS has been reported in case of relatively large Schottky barrier heights (0.9eV) [60, 61] and moderately large barrier heights (0.83eV) [62], using forward bias voltage pulses in the latter case. Comparable conditions are given in Cu(In,Ga)(S,Se)<sub>2</sub>-based heterojunctions, because the observation of a type inversion at the (in-vacuo) Cu(In,Ga)Se<sub>2</sub> surface [21] indicates a high

band bending. Thus, bulk minority-carrier defect states *can* be detected in Cu(In,Ga)(S,Se)<sub>2</sub> heterojunctions and Schottky contacts even without minority-carrier filling pulses.

### Influence of Series Resistance and Leakage Current

Most capacitance bridges apply an equivalent circuit of a parallel configuration of a capacitor (capacitance  $C_p$ ) and a resistor (resistance  $R_p = G^{-1}$  (inverse conductance)). A series resistance  $R_s$ , caused by contact resistances and the sheet resistance of the window layer, is usually negligible. In this case, the measured capacitance  $C_p$  corresponds to the actual sample capacitance. However, if the sample is highly resistive or the leakage current is negligible, the appropriate equivalent circuit is a capacitor (capacitance  $C_s$ ) in series with a resistor (resistance  $R_s$ ). The quality factor  $Q$  provides a measure to which extent a series resistance influences the capacitance measurement performed in the parallel equivalence configuration,

$$Q = R_s C_s \omega. \quad (3.20)$$

Here,  $\omega$  denotes the circle frequency of the alternating voltage applied by the capacitance bridge ( $2\pi \times 1\text{MHz}$  for the Boonton 7200 capacitance meter used in our transient-DLTS setup). The measured capacitance  $C_p$  is related to the series capacitance  $C_s$  by

$$C_p = \frac{C_s}{1 + Q^2} \quad (3.21)$$

and, thus, depends on the width of the depletion region [63]. For DLTS, the change  $\delta C_p$  related to  $\delta C_s$  in the first order is

$$\delta C_p = \frac{1 - Q^2}{(1 + Q^2)^2} \delta C_s. \quad (3.22)$$

The correction factor  $\delta C_p / \delta C_s$  equals one at  $Q = 0$ , but changes rapidly to zero for  $Q = 1$  and remains negative for  $Q > 1$  [64]. Thus, for highly resistive samples, the DLTS signal is reduced in amplitude and possibly changed in sign.

Chen et al. [65] have studied the influence of high leakage currents on DLTS spectra using Cr–Au/SiN/GaAs metal–insulator–semiconductor capacitors with a very thin SiN layer (5nm). The dc leakage current density at  $T = 300\text{K}$  and  $-1\text{V}$  bias voltage was about  $5\mu\text{A}/\text{cm}^2$ . The authors state that thermally activated leakage causes the competition of carrier capture in the space charge region with the thermal emission from energy-distributed defect states, thus, changing the trap occupancy. The high-temperature side of the resulting DLTS spectrum is cut off, shifting the peak position and reducing the peak amplitude, the latter then being approximately linearly dependent on the rate window.

### 3.2.3 Capacitance–Voltage Measurement

A Capacitance–Voltage ( $C$ – $V$ ) measurement is useful for determining the doping density and its depth profile of a p–n or Schottky junction. The capacitance  $C$  in dependence on the applied voltage  $V$  can be written in a simple expression, if the thermal energy  $kT$  is much smaller than the band bending  $V_{bi} - V$  and the depletion approximation is assumed.

$$C = A \sqrt{\frac{e\epsilon_s}{2} \frac{|N_A - N_D|}{(V_{bi} - V) - \frac{kT}{e}}}, \quad (3.23)$$

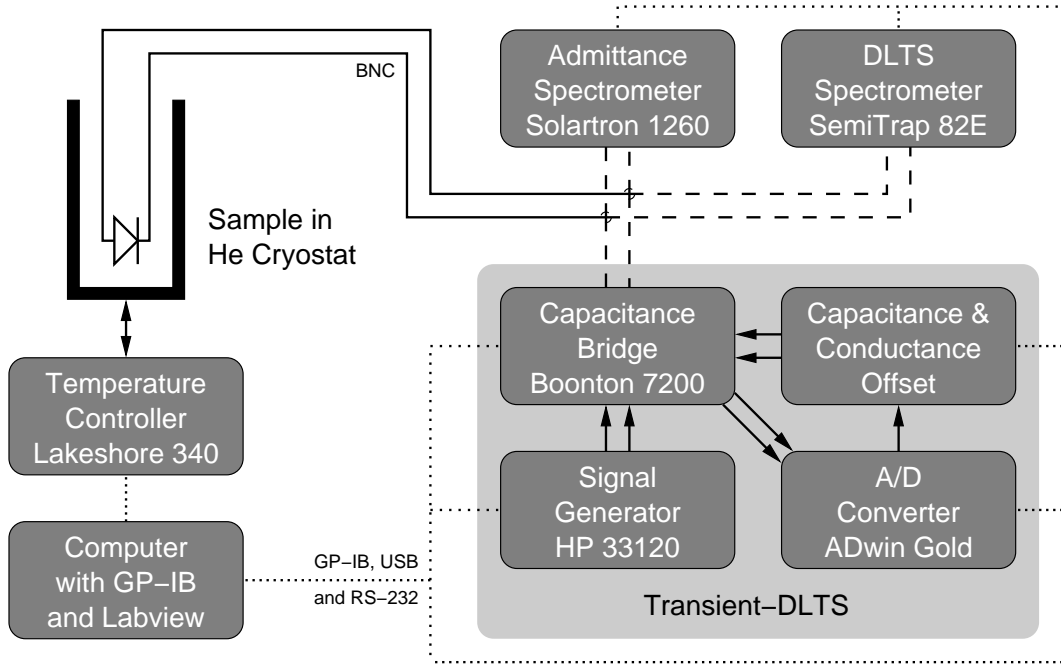


**Figure 3.5:** The experimental setup used for capacitance spectroscopy.

where  $A$  is the active area of the junction,  $\epsilon_s$  the dielectric constant of the semiconductor,  $e$  the electron charge, and  $V_{bi}$  the junction built-in electronic potential. A plot of  $1/C^2$  versus the applied bias  $V$ , the so-called Mott-Schottky plot, has a slope proportional to the net doping density  $|N_A - N_D|$  and an abscissa intercept of  $V_{bi} - kT/e$ , if the doping profile is uniform, and no deep traps are present. The local voltage derivative of the Mott-Schottky relation is proportional to the local net doping density  $|N_A - N_D|(W)$  at the edge of the space charge region,  $W$ ,

$$|N_A - N_D|(W) = -\frac{2}{\epsilon_s e A^2} \left( \frac{d(1/C^2)}{dV} \right)^{-1}. \quad (3.24)$$

If the sample contains defect states in high concentrations, say, larger than a tenth of the net doping density, they have to be considered in the evaluation of the  $C$ - $V$  measurements. A concise formulation can be found in Ref. [42]. An alternative to minimize the influence of deep traps followed in this thesis is to perform the capacitance-voltage measurements at low temperatures, where the deep defect states cannot respond to the fast alternating voltage of the capacitance meter. The validity is verified by admittance spectroscopy.

### 3.3 Experimental Equipment

The modification of the solar cell parameters of the samples have been characterized using current-voltage measurements under AM 1.5 (solar spectrum) illumination at  $25^\circ\text{C}$  ambient temperature. Temperature-dependent current-voltage characteristics were performed using a Keithley 236 source measuring unit. Admittance spectroscopy measurements were performed using a Solartron 1260 impedance analyzer, operating with an alternating voltage of 30mV amplitude at frequencies in the range between 1Hz and 1MHz. In order to look



at the interface properties of the samples, I have varied the external voltage from zero to reverse bias ( $-2\text{V}$ ). Capacitance–voltage measurements were carried out at  $T = 90\text{K}$  and a frequency of  $100\text{kHz}$ . DLTS was done by applying two spectrometers, a conventional Semitrap 82E apparatus (using a hardware lock-in amplifier to evaluate the transients) and a custom-built [58] transient-DLTS based on a Boonton 7200 capacitance meter. The Semitrap spectrometer applies a fixed alternating voltage amplitude of  $100\text{mV}$ , the transient-DLTS setup can be adjusted in the range  $15\text{--}100\text{mV}$ . In both cases, the sampling frequency for measuring the transients of the sample capacitance is  $1\text{MHz}$ . The transient-DLTS allows control over each parameter using a computer. Capacitance and conductance were measured every  $10\mu\text{s}$ , up to a total length of  $1.5\text{s}$  ( $15000$  data points). The resulting transients were evaluated using exponential fits or the Laplace transformation method [66]. Temperature-dependent analysis was performed using a liquid helium closed-cycle cryostat in the range from  $20\text{K}$  to  $350\text{K}$ . In order to minimize the slow relaxation of the light soaking [27], we anneal the samples at  $350\text{K}$  for half an hour in helium gas atmosphere prior to the measurements. The experimental setup is illustrated schematically in Figure 3.5.

Details about the origin of defect states in  $\text{Cu}(\text{In,Ga})(\text{S,Se})_2$  are still mostly unknown. Numerical calculations studying the defect physics of  $\text{CuInSe}_2$ -related compounds are mainly concerned with the formation and activation energies of defects and defect complexes [32]. Since, to my knowledge, the temperature dependence of the capture cross-section of deep states in the above material has not been studied yet, I assume the capture cross-section to be temperature independent, in order to simplify the analysis. I follow the custom of researchers in that material class [52, 67, 68] and neglect both the degeneracy and the entropy factor [69]. These simplifications imply that the values of the activation energy determined might be somewhat distorted. Consequently, the temperature-dependent emission rate, being the finger print of the related defect state, is the most reliable quantity for comparing electronically determined defect states with each other.

The statements whether a defect state is acceptor-like or donor-like is based on the detection of a minority-carrier or majority-carrier DLTS-signal, also taking the type of doping of the investigated semiconductor layer into account. We note that this assignment is only a highly probable assumption, also regarding the calculations by Zhang et al. [32]. However, there remains a small chance that, e.g., a majority-carrier defect state in a p-doped semiconductor layer is donor-like and not (as assumed here) acceptor-like.



# 4 Experimental Results

The electrical characterization of the  $\text{Cu}(\text{In,Ga})(\text{S,Se})_2$ -based solar cells and Schottky contacts in both, as-grown and DH treated state, is described subsequently. A general overview of the changes of the solar cell parameters (e.g., the open-circuit voltage) and material characteristics (e.g., doping density and series resistance) is given in Section 4.1. The application of capacitance spectroscopy allows for an extensive investigation of the alteration of interface (Section 4.2) and bulk defect states (Section 4.3) due to DH treatment.

## 4.1 General Observations

Current–voltage measurements are suitable for macroscopically monitoring changes of the heterojunction charge transport properties. The effect of exposing the non-encapsulated  $\text{Cu}(\text{In,Ga})(\text{S,Se})_2$ -based heterojunction samples to  $\text{H}_2\text{O}$  vapor is manifested in losses in the fill factor and the open-circuit voltage, whereas the short-circuit current density remains almost unaffected, as illustrated in Figure 4.1(a). We note that the change in open-circuit voltage for samples with DH treated absorbers is very similar to that of cells that are DH-treated after deposition of the CdS buffer or the i-ZnO window layer. The effect of annealing in dry air at  $85^\circ\text{C}$  for 24h on the electronic properties is fully reversible.

A hysteresis of the current–voltage characteristics at forward bias can be observed for heterojunction devices and  $\text{Cr}/\text{Cu}(\text{In,Ga})(\text{S,Se})_2$  Schottky contacts (Figure 4.1(b)) only after DH exposure, when the direction of the voltage sweep is changed. This voltage hysteresis indicates a charging effect within the absorber layer. From the temperature-dependent saturation current density, corrected by the ideality factor, we determine Schottky barrier heights ranging from 0.6V to 0.8V.

Impedance measurements performed at different bias voltages ( $-1.5\text{V}$ – $0.5\text{V}$ ) on the  $\text{Cu}(\text{In,Ga})(\text{S,Se})_2$ -based solar cells, represented in the form of Nyquist plots, show only one semi-circle, i.e., only one space charge region. At  $T = 300\text{K}$ , the parallel resistance at zero bias diminishes from  $10\text{k}\Omega$  in the as-grown samples to about  $2\text{k}\Omega$  after 438h of DH treatment. The resistances obtained from the current–voltage characteristics are lower by about a factor of two.

The current–voltage and capacitance–voltage measurements performed before and after DH testing do not indicate the formation of a back-contact barrier for samples exposed to DH conditions as fully processed devices, a problem commonly reported for the case of standard CdTe solar cells [70]. Samples exposed to DH conditions after an interruption of the processing, however, show transport problems in forward bias.

The effective doping density of the  $\text{Cu}(\text{In,Ga})(\text{S,Se})_2$  based heterostructure samples was determined using capacitance–voltage ( $C$ – $V$ ) measurements. These experiments were per-

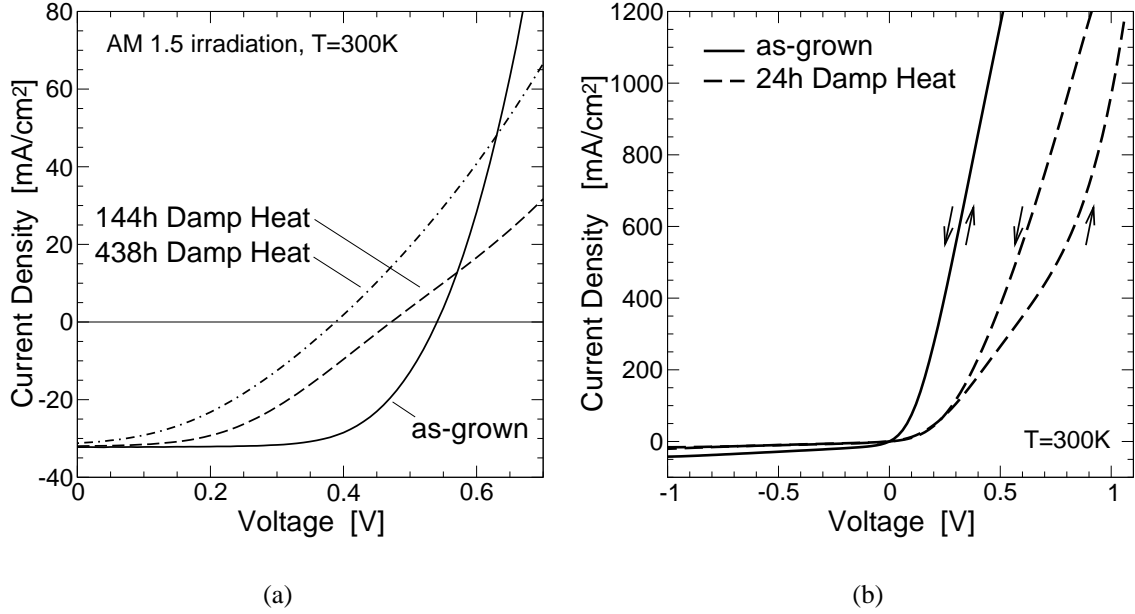


**Figure 4.1:** Current–voltage characteristics of (a)  $\text{Cu}(\text{In,Ga})(\text{S,Se})_2$ -based heterojunction solar cells under AM 1.5 irradiation and (b)  $\text{Cr}/\text{Cu}(\text{In,Ga})(\text{S,Se})_2$  Schottky contacts. The hysteresis is also observed in DH treated solar cells.

formed at 90K ambient temperature and 100kHz frequency, in order to minimize the influence of deep levels, which then cannot follow the capture–emission processes (induced by the alternating voltage applied in capacitance measurements) and, thus, do not contribute to the capacitance signal. The slope of the resulting Mott-Schottky plots ( $1/C^2$  versus  $V$ ) clearly shows that the net doping concentration diminishes from  $5.5 \times 10^{15} \text{cm}^{-3}$  for as-grown cells to about  $2.5 \times 10^{15} \text{cm}^{-3}$  for cells after 144h of DH treatment [71]. At  $T = 300\text{K}$ , effective doping densities of about  $1.3 \times 10^{16} \text{cm}^{-3}$  are found for as-grown samples, whereas samples exposed to DH for 144h still show about  $2.5 \times 10^{15} \text{cm}^{-3}$ . At both temperatures, the slope of the Mott-Schottky plots is slightly nonlinear, indicating a nonuniform distribution of the doping levels and, for 300K ambient temperature, the possible influence of trap states.

## 4.2 Interface Defect States

Applying capacitance spectroscopy, we observed two interface defect states,  $\beta$  and  $\theta$ .  $\beta$  is found in each heterojunction and Schottky contact that was investigated. The defect state  $\theta$  is clearly detected only after 438h of DH treatment.

### 4.2.1 Interface Defect State $\beta$

The activation energy of interface defect states is determined by the difference between the quasi-Fermi level and the corresponding energy band. In the case of the heterojunction devices, we identify such a defect state with admittance spectroscopy, minority-, majority-, and reverse-DLTS, respectively [41, 71]. The corresponding admittance spectra are shown

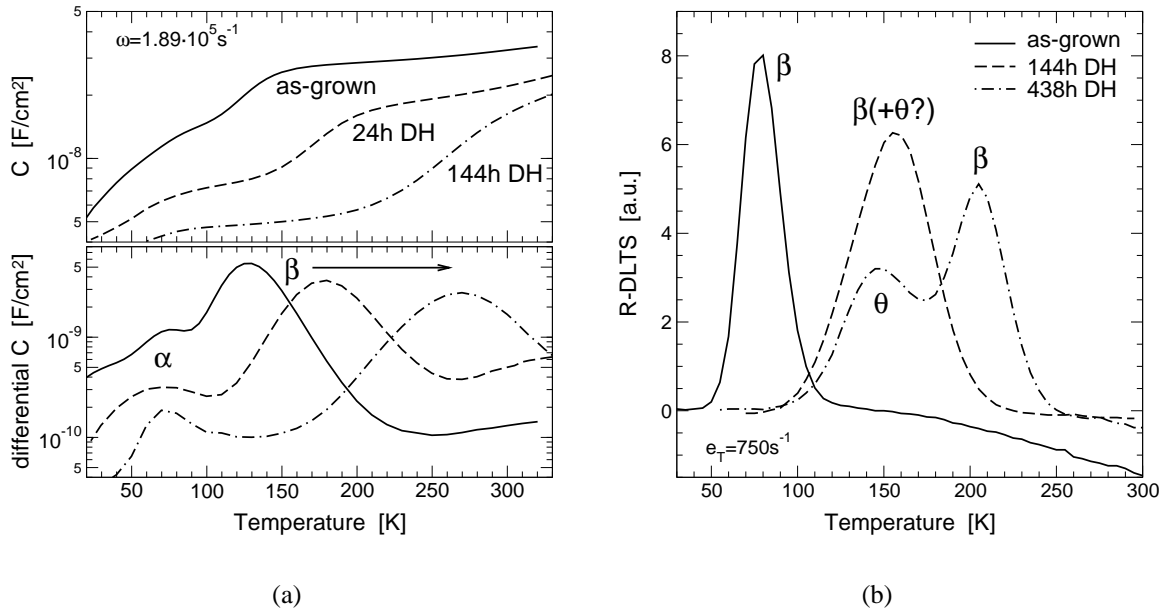


**Figure 4.2:** (a) Capacitance and differentiated (with respect to frequency) capacitance versus temperature of as-grown and DH treated (24h and 144h) heterostructure samples. The interface defect state  $\beta$  is shifted with time elapsed under DH conditions. (b) R-DLTS spectrum (recorded with the conventional DLTS system) versus temperature of the as-grown and DH treated (144h and 438h) Cu(In,Ga)(S,Se)<sub>2</sub>-based solar cells. The shift of the interface defect state  $\beta$  and the evolving of the defect state  $\theta$  after 438h DH exposure are observed.

in Figure 4.2(a), the R-DLTS spectra in Figure 4.2(b).  $\beta$  is located presumably at the buffer/absorber interface [52, 71]. The origin and magnitude of the activation energy of  $\beta$ ,  $\Delta E$ , are indicated in a band diagram of the n-ZnO/i-ZnO/CdS/Cu(In,Ga)(S,Se)<sub>2</sub> heterostructure, see Figure 5.1 in the next chapter. The temperature-dependent emission rates of the defect state  $\beta$  are assembled in an Arrhenius representation (Figure 4.3). The defect parameters are summarized in Table 4.1.

Samples exposed to the DH environment show a continuous shift of the activation energy and capture cross-section of the interface state  $\beta$  proportional to the exposure time [71, 72]. We note that the amplitude of the capacitance step related to  $\beta$  decreases proportional to the shift of the activation energy [73]. We cannot determine the defect concentration quantitatively for reasons discussed in Section 3.2.1. The main part of the shift of  $\beta$  proves to be irreversible in the case of DH treated solar cells and samples with DH exposed absorber layer, but is completely reversible at dry air annealing of the absorber layer at 85°C. Herberholz et al. [52] observed an irreversible shift of  $\beta$  (called N2 therein) after repetitive air annealing for up to two minutes at 240°C. The reversible part of the shift of  $\beta$  can be influenced by light soaking [27]. We determine a relaxation time of about 10 days from the light-soaked<sup>1</sup> to the relaxed state. By annealing at  $T = 350\text{K}$  in helium gas atmosphere, the relaxed state can be reached in about half an hour. This persistent photoconductivity was formerly explained with

<sup>1</sup>Prolonged illumination of the samples is denoted as light soaking.

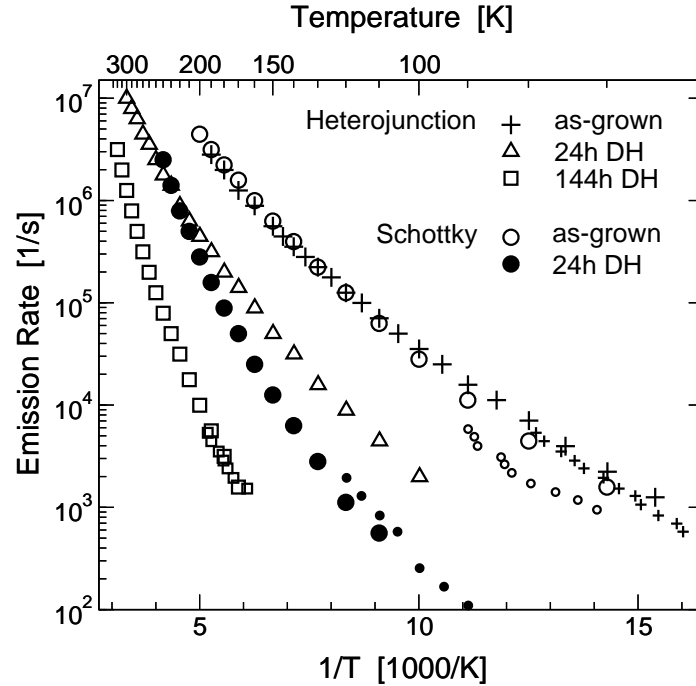


**Figure 4.3:** Arrhenius representation of the temperature-dependent emission rates of the interface defect state  $\beta$ . The data was obtained from heterostructure samples and Schottky contacts. The emission rates of the as-grown states of the  $\text{Cu}(\text{In,Ga})(\text{S,Se})_2$ -based solar cells and the  $\text{Cr}/\text{Cu}(\text{In,Ga})(\text{S,Se})_2$  Schottky contact are very similar. Large symbols denote data obtained by admittance spectroscopy, small symbols represent DLTS data.

a large lattice relaxation [74], found also in the DX center in GaAs compounds [75, 76].

In DLTS,  $\beta$  is extracted from a minority-carrier signal, i.e., the space charge width is reduced directly after the termination of the filling pulse. The DLTS signal of  $\beta$  can be clearly observed with minority, majority and reverse-DLTS. Thus, we note that the observation of  $\beta$  does not depend on the injection of minority carriers.

We were able to observe the defect state  $\beta$  in all investigated  $\text{Cu}(\text{In,Ga})(\text{S,Se})_2$ -based solar cells (with CdS and ZnSe buffer layer) and  $\text{Cr}/\text{Cu}(\text{In,Ga})(\text{S,Se})_2$  Schottky junctions, for both, as-grown and DH-treated absorbers [41]. The admittance spectra of the Schottky contacts are displayed in Figure 4.4 (DLTS not shown here), the Arrhenius plots in Figure 4.3: The typical shift of the defect state  $\beta$  to higher activation energies due to DH treatment is recognized again. The characteristics are comparable to heterojunction cells, where only the absorber layer was exposed to DH conditions [73].

As-grown  $\text{Cu}(\text{In,Ga})(\text{S,Se})_2$ -based solar cells usually show Fermi-level pinning at the buffer/absorber interface [52, 68, 71]. The influence of DH treatment on devices that are exposed to the test conditions with the complete heterostructure gives rise to an unpinning of the Fermi level, which manifests in a shift of the interface state  $\beta$  when applying an external bias voltage [71], as can be seen in Figure 4.5. Devices containing DH treated absorbers, however, still show Fermi-level pinning [71]. We note that in as-grown samples, the emis-

Sample	Activation Energy [meV]	Attempt-to-Escape Frequency [Hz]	Capacitance Step Height [nF/cm <sup>2</sup> ]
heterojunction as-grown	50	$7.4 \times 10^7$	12.5
heterojunction 24h DH	85	$3.6 \times 10^8$	9.0
heterojunction 144h DH	195	$8.9 \times 10^9$	5.8
heterojunction 294h DH	280	$1.8 \times 10^{11}$	4.8
heterojunction 438h DH	315	$1.1 \times 10^{12}$	2.9
heterojunction 6h absorber DH	170	$2.2 \times 10^9$	5.0
heterojunction 24h absorber DH	160	$1.6 \times 10^9$	5.4
Schottky as-grown	55	$2.3 \times 10^8$	5.3
Schottky 24h DH	120	$1.7 \times 10^9$	6.6

**Table 4.1:** Activation energy  $\Delta E$ , attempt-to-escape frequency  $\nu_0$ , and capacitance step height  $\Delta C$  of the defect state  $\beta$  for various sample configurations (as-grown and DH-treated heterojunctions and Schottky contacts).

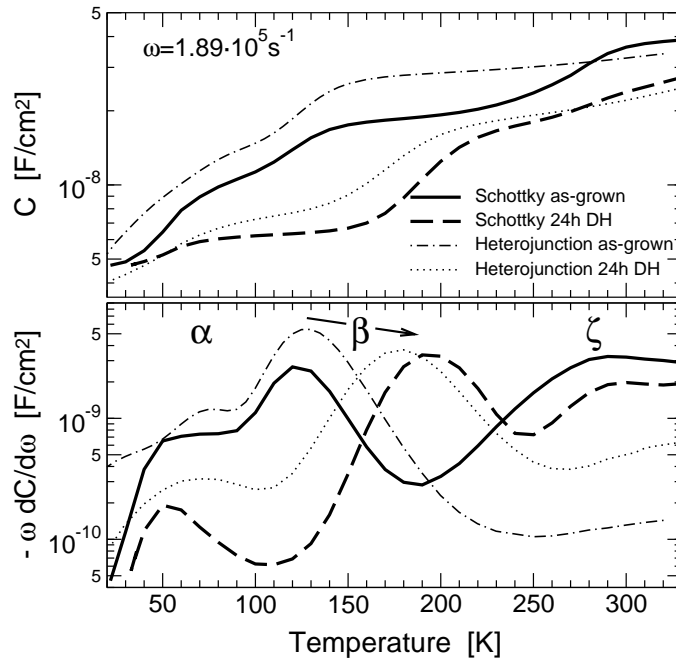


**Figure 4.4:** Capacitance and differentiated (with respect to frequency) capacitance versus temperature of as-grown and DH treated (24h) Cr/Cu(In,Ga)(S,Se)<sub>2</sub> Schottky contacts. The corresponding spectra of the heterostructure samples are shown as well.

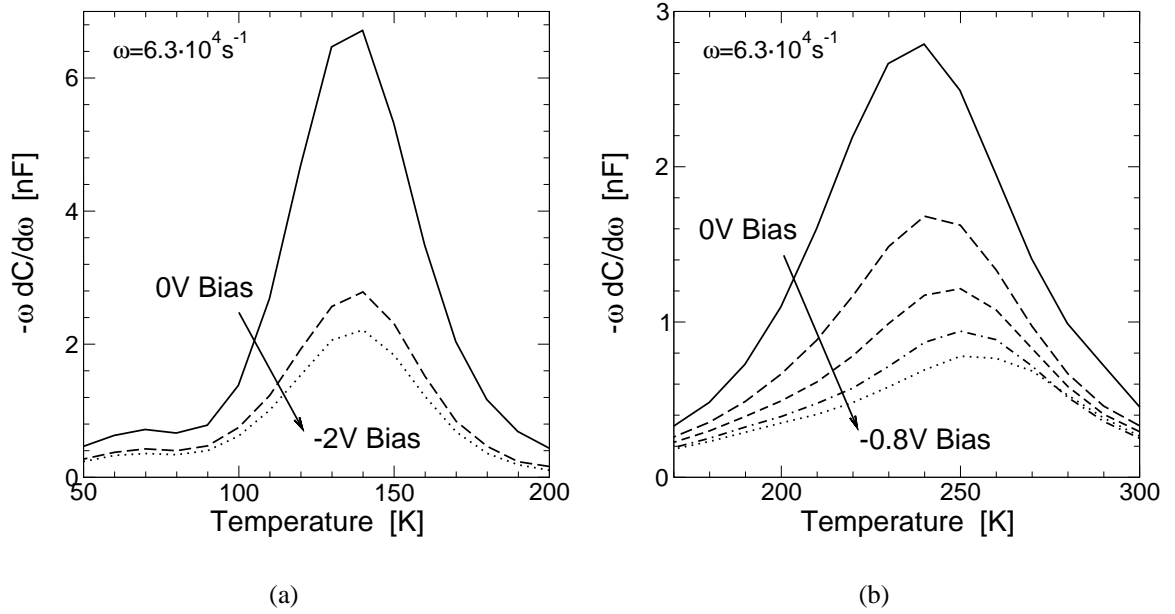


**Figure 4.5:** Differentiated (with respect to frequency) capacitance versus temperature spectra of (a) as-grown and (b) DH treated  $\text{Cu}(\text{In,Ga})(\text{S,Se})_2$ -based heterojunctions, with different external reverse biases applied. The unchanged peak position of  $\beta$  in the as-grown sample signifies a Fermi-level pinning. After DH treatment, the peak position shifts with the external reverse bias: the Fermi level is unpinned.

sion rates of  $\beta$  do not depend on the bias voltage (admittance spectroscopy and DLTS) and pulse height (DLTS), i.e.,  $\beta$  is observed irrespective of the extent of the space charge region.

#### 4.2.2 Interface Defect State $\theta$

A defect state  $\theta$  can be identified after 438h DH treatment of the whole device with the help of R-DLTS, as can be seen in Figure 4.2(b). We determined an activation energy of about 140meV. Since the heterojunction samples do not contain a single-sided abrupt p-n junction, both edges of the space charge region contribute to the DLTS signal, confounding the determination of the spatial origin of the defect state  $\theta$ . Taking into account that the shift of  $\beta$  for the above DH treated sample (438h) indicates a position of the Fermi level of about 300meV below the conduction-band minimum, the defect state  $\theta$  would be too shallow to be detected, in case it were located in the absorber layer or at the buffer/absorber interface. Further,  $\theta$  cannot originate from the n-type region, because a minority-carrier trap could not be observed using capacitance spectroscopy at a position of 140meV above the valence-band maximum. Thus, the defect state  $\theta$  presumably is an interface state located at the CdS/ZnO interface or an internal grain boundary of the absorber.



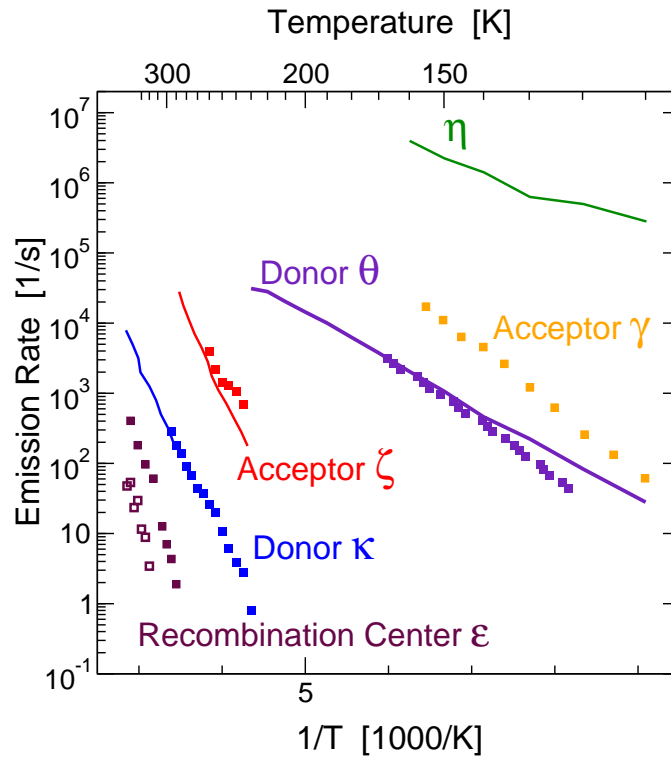


**Figure 4.6:** The Arrhenius representation of the temperature-dependent emission rates of the bulk traps and the interface defect state  $\theta$  found in the heterostructure samples and Schottky contacts. Solid lines denote admittance spectroscopy data, dots denote DLTS measurements. For the midgap center  $\varepsilon$ , the majority (full symbols) and minority carrier response (open symbols) are presented.

## 4.3 Bulk Defects

With the help of capacitance spectroscopy, several bulk defect states located inside the heterostructure devices can be observed. In the following, we will describe all defect states detected, focussing on those which seem to be related to the changes of the electrical characteristics of cells exposed to the DH conditions. The defect characteristics are summarized in Table 4.2. The temperature-dependent emission rates of the bulk traps and the interface defect state  $\theta$  are displayed in the Arrhenius plot of Figure 4.6.

For all samples, we estimate the Q-factor [63] (i.e., a measure for the influence of the series resistance on the DLTS spectra) to be much smaller than unity: the DLTS signals of as-grown and DH treated samples are not inverted.

### 4.3.1 Recombination Center $\varepsilon$

A deep defect state,  $\varepsilon$ , is observed in DLTS spectra recorded before and after DH treatment, in conventional and transient-DLTS. We observe minority and majority DLTS signals (depending on the amount of injected minority carriers during the application of the filling

Defect State	Trapped Charge Carrier	Activation Energy [meV]	Capture Cross-Section [cm <sup>2</sup> ]
$\gamma$	hole	270	$10^{-14}$
$\zeta$	hole	380	$10^{-14}$
$\kappa$	electron	480	$10^{-15}$
$\varepsilon$	hole / electron	midgap	$10^{-15}$
$\eta$	(unknown)	55	$10^{-18}$
$\theta$	electron	105	$10^{-19}$

**Table 4.2:** Parameters of the bulk defect states. The values of the activation energy and the capture cross-section have been determined from the Arrhenius data. Bear in mind that the capture cross-sections determined by this method are quite inaccurate.

pulse), both of them resulting in activation energies of about 550meV. Consequently, we expect the defect state  $\varepsilon$  to be a midgap recombination center. Its capacitance transient at 350K for the case without injection pulses can be seen in Figures 4.7(a) and 4.7(b) for as-grown samples and cells exposed to DH conditions for 144h, respectively. Other groups observed a majority-carrier trap of similar emission rates in single crystalline CuInSe<sub>2</sub> solar cells with (Cd,Zn)S buffer layer [77, 78, 79]. They determined an activation energy of about 500meV.

The normalized amplitude  $\Delta C/C_0$  of the capacitance transient related to  $\varepsilon$  is diminished due to the DH treatment. The determination of the trap concentration is complicated by several circumstances: First, the transient amplitude strongly depends on temperature, indicating the influence of a temperature-dependent capture cross-section or leakage currents (especially for the DH treated device) on the amplitude [65]. Second, the prerequisite for an accurate DLTS analysis,  $\Delta C/C_0 \ll 1$  [11], does not hold for the transient of the as-grown sample. Third, the first 120 $\mu$ s of the transient cannot be detected due to the finite response time of the capacitance bridge. Fourth, the transient is non-exponential. Fifth, amplitude and decay strongly depend on the width of the filling pulse. For comparison purposes, we use the standard relation for determining the concentration [11], bearing in mind that we obtain only an ‘apparent concentration’ (in the single-electron model) due to the circumstances mentioned above. For  $\varepsilon$  at 350K, we multiply the normalized amplitude at  $t = 130\mu$ s with the corresponding net doping concentration. For a filling pulse width of 100 $\mu$ s, we find  $2 \times 10^{14}\text{cm}^{-3}$  of  $\varepsilon$  in the as-grown state and an upper limit of about  $10^{13}\text{cm}^{-3}$  for the DH treated sample. For a pulse width of 1s, the amplitudes are nearly saturated, and we obtain an apparent concentration of  $5 \times 10^{14}\text{cm}^{-3}$  for as-grown samples and  $2 \times 10^{14}\text{cm}^{-3}$  for samples exposed to DH. A donor-like defect state of similar emission rates which shows an increased concentration after DH exposure has been observed by Igalson et al. [67]. It is unclear whether this defect state corresponds to the minority-carrier signal of  $\varepsilon$  or to the donor-like defect state  $\kappa$  (Section 4.3.4).

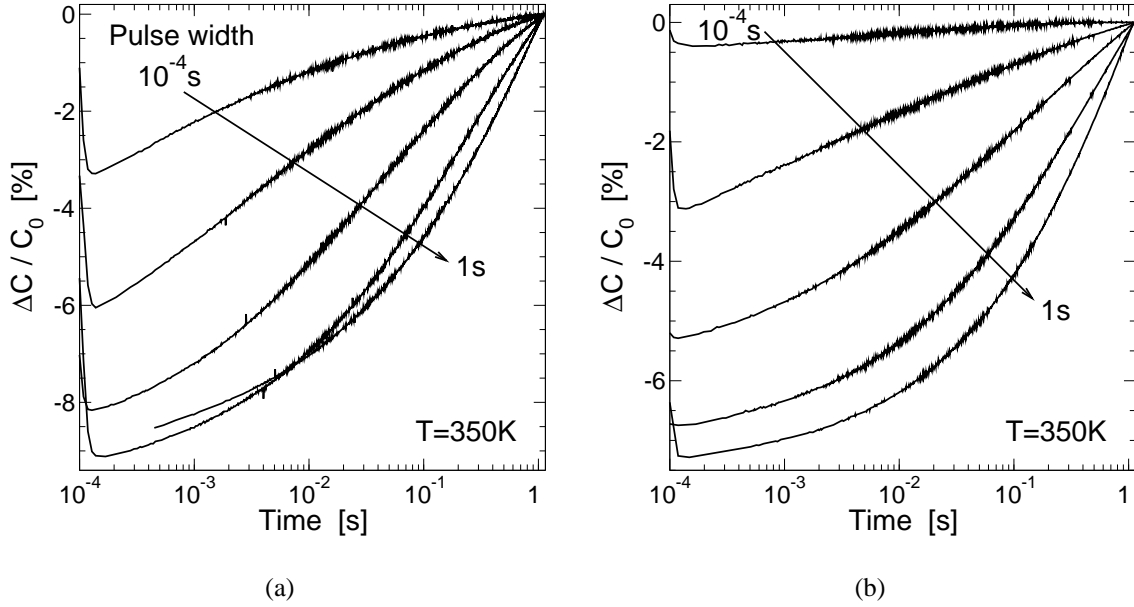


**Figure 4.7:** Capacitance transients of (a) as-grown and (b) DH treated (144h)  $\text{Cu}(\text{In,Ga})(\text{S,Se})_2$  heterojunction at  $T = 350\text{K}$ . The 1.5V filling pulse with a width ranging from  $100\mu\text{s}$  to 1s was superimposed on a quiescent reverse bias of -1.5V.

### 4.3.2 Acceptor-like Defect State $\gamma$

We observe an acceptor-like defect state,  $\gamma$ , with conventional and transient-DLTS in as-grown samples only. The corresponding capacitance transient at  $T = 125\text{K}$  is shown in Figure 4.8(a); it is non-exponential. We determine an activation energy of approximately 160meV. The capacitance transient of a DH treated sample (144h) is shown for comparison in Figure 4.8(b). Similar to  $\epsilon$ , the normalized amplitude  $\Delta C/C_0$  is diminished due to the DH treatment. An estimation of the concentration, under the same conditions and limitations as described above, yields  $2 \times 10^{14}\text{cm}^{-3}$  for as-grown samples at  $T = 125\text{K}$ , for both filling pulse widths,  $100\mu\text{s}$  and 1s, i.e., the trap is already saturated for the shorter time. We obtain an upper limit for the apparent concentration after the DH treatment of  $10^{13}\text{cm}^{-3}$  for a pulse width of  $100\mu\text{s}$ . For a filling pulse width of 1s, the amplitude becomes positive: a superposition with the shifted minority-carrier signal  $\beta$  takes place. This overlapping makes a determination of the concentration of  $\gamma$  impossible, and also puts in question the concentration determined for the short pulse width.

### 4.3.3 Acceptor-like Defect State $\zeta$

A deep acceptor-like defect state,  $\zeta$ , was detected with admittance spectroscopy and DLTS in as-grown and DH treated Schottky contacts, and in samples containing absorbers exposed to DH conditions. In samples DH treated as complete heterostructure, we observed a feature close to the position of  $\zeta$  with conventional and transient-DLTS, with a non-exponential decay and a relatively small amplitude. The defect state is related to the fast decay of the

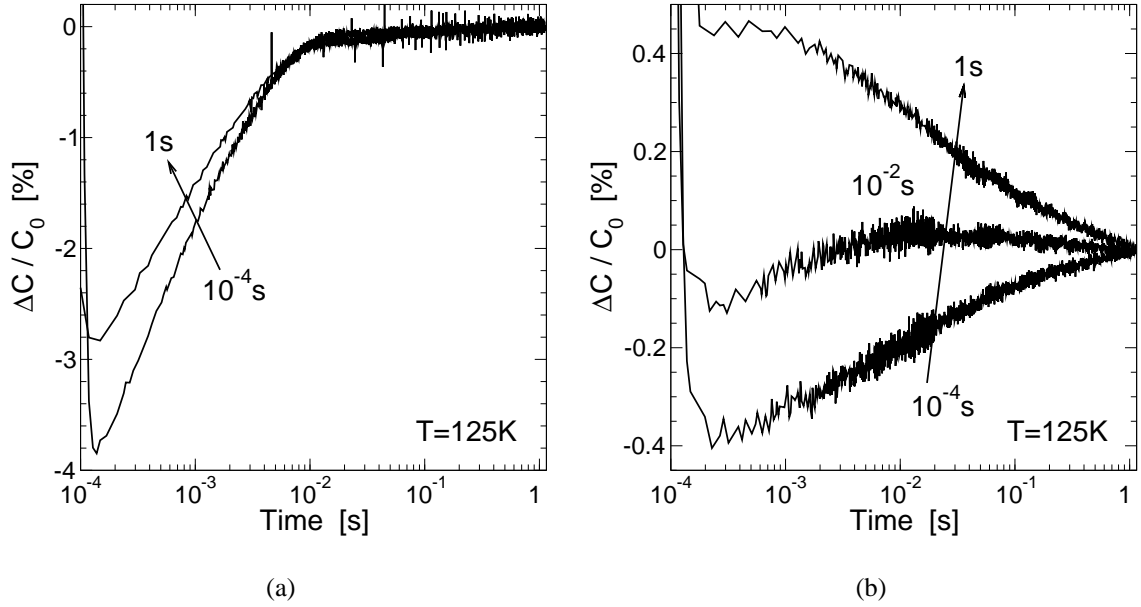


**Figure 4.8:** Capacitance transients of (a) an as-grown and (b) a DH treated (144h)  $\text{Cu(In,Ga)(S,Se)}_2$ -based heterojunction at  $T = 125\text{K}$ . The 1.5V filling pulse with a width ranging from  $100\mu\text{s}$  to 1s was superimposed on a quiescent reverse bias of -1.5V.

capacitance transient of the DH treated sample at  $T = 200\text{K}$ , shown in Figure 4.9(b). The apparent concentration of about  $10^{13}\text{cm}^{-3}$  is almost independent of the pulse width. We note that a yet unidentified majority-carrier signal of slightly lower concentration becomes visible for increasing filling pulse widths. The defect state  $\zeta$  vanishes in the background in as-grown samples (Figure 4.9(a)), therefore statements concerning the concentration change due to DH treatment are made impossible by an upper limit of  $1.5 \times 10^{13}\text{cm}^{-3}$  (due to the background). From the admittance data, we obtain an activation energy of about 380meV for  $\zeta$ . Note that in co-evaporated  $\text{CuInSe}_2$ -based cells, the defect state  $\zeta$ , also referred to as N2, is present with high concentration already in the as-grown state, such that it can easily be detected using admittance spectroscopy [52]. In that cell type, its concentration is proportional to the time elapsed under DH conditions [72]. This defect state was also observed in single-crystalline  $\text{CuInSe}_2$ -based solar cells with (Cd,Zn)S buffer layer [78].

#### 4.3.4 Defect State $\kappa$

The acceptor-like defect state  $\kappa$  is detected with admittance spectroscopy and DLTS in samples with modified absorber stoichiometry, i.e., Na poor, Cu rich and Cu+Na rich absorbers [80], and in Schottky contacts with a Cu rich  $\text{Cu(In,Ga)(S,Se)}_2$  layer. In these devices,  $\kappa$  is the dominant bulk trap, as it is present in relatively high concentrations. However, we observe no sign of  $\kappa$  in as-grown and DH treated samples with standard stoichiometry.

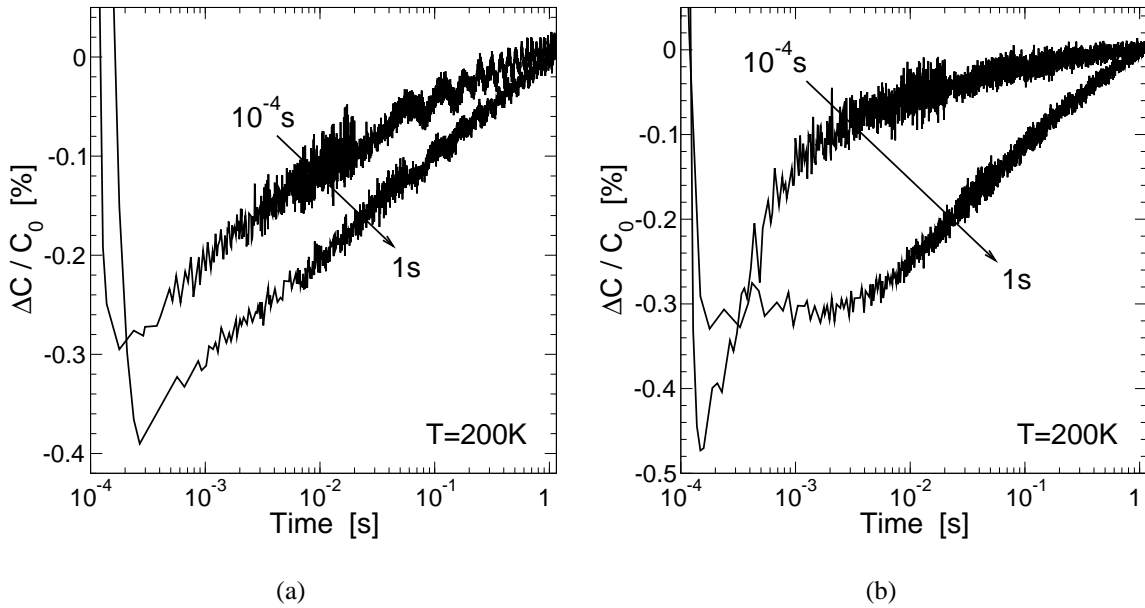


**Figure 4.9:** Capacitance transients of (a) an as-grown and (b) a DH treated (144h)  $\text{Cu}(\text{In,Ga})(\text{S,Se})_2$ -based heterojunction at  $T = 200\text{K}$ . The 1.5V filling pulse with a width ranging from  $100\mu\text{s}$  to 1s was superimposed on a quiescent reverse bias of -1.5V.

#### 4.3.5 Defect State $\eta$

The defect state  $\eta$  features high emission rates already at low temperatures and, thus, can be detected with admittance spectroscopy only. Its capacitance step height is about a factor of 20 lower than that of  $\beta$ . Consequently, the defect state  $\eta$  is observed only if  $\beta$  is shifted relative to its position in reference samples, e.g., after DH treatment. The activation energy of  $\eta$  is about 55meV. Its spatial location and origin remain unclear.



# 5 Numerical Simulations

Calculations of the possible loss factors prominent in DH treated Cu(In,Ga)(S,Se)<sub>2</sub>-based solar cells were carried out using the one-dimensional device simulation program SCAPS [81] developed by M. Burgelman and A. Niemegeers. This program allows to simulate illumination and temperature dependent current–voltage, capacitance–voltage, admittance spectroscopy, and quantum efficiency measurements. The corresponding band diagrams are calculated as well.

The simulations are based on the numerical solution of coupled continuity equations for free charge carriers and the Poisson equation, in order to calculate the charge carrier and current densities in each semiconductor layer. The boundary conditions between two adjacent semiconductor layers are given by the model of thermal emission. Interface recombination is also accounted for, also considering recombination of charge carriers in the valence band of one semiconductor layer with charge carriers in the conduction band of an adjacent semiconductor layer [82]. In the case of metal/semiconductor interfaces, thermal emission of majority carriers and an effective interface recombination velocity for minority carriers are considered. Bulk defect states are described by the Shockley–Read–Hall recombination model [44, 45]. Tunneling of charge carriers is not taken into consideration.

Details of the SCAPS simulation parameters used and the calculated results of the n-ZnO/i-ZnO/CdS/Cu(In,Ga)(S,Se)<sub>2</sub>/Mo solar cell parameters can be found in Appendix C. The i-ZnO layer is taken into account with two alternative doping densities,  $10^{15}\text{cm}^{-3}$  and  $10^{18}\text{cm}^{-3}$  (in the following also denoted as low and high i-ZnO doping concentration). Niemegeers et al. [68] have used a relatively high doping concentration of  $10^{18}\text{cm}^{-3}$  for their calculations. However, Palm [83] determined the sheet resistance of i-ZnO on glass to be at least 7 orders of magnitude higher than n-ZnO on glass. Of course, the doping density of i-ZnO in the fully processed heterostructure could be influenced by the adjacent layers (possibly even the dopant of the n-ZnO layer), but we were not able to determine it. Thus, we verify the numerical simulations by using  $10^{15}\text{cm}^{-3}$  as alternative i-ZnO doping density. Only qualitative descriptions of the numerical simulations are given. We point out that the significance of the numerical simulations is limited by the estimation of many unknown parameters for this material system.

## 5.1 On the Validity of the Open-Circuit Voltage Extrapolation Method

The crucial question whether the recombination at the buffer/absorber interface or in the bulk of the chalcopyrite layer plays a dominant role cannot be answered directly. The method

of extrapolating the open-circuit voltage to  $T = 0\text{K}$  has been applied in earlier publications [71, 72] in order to determine the major recombination path. It yielded the absorber bandgap energy, thus, in principle, indicating predominant recombination in the space charge region. For verification, we used SCAPS to calculate the temperature-dependent open-circuit voltages for two hypothetical sample definitions, one with bulk traps only, and the other with exclusively interface defect states. In both cases, the extrapolation of the open-circuit voltage to  $T = 0\text{K}$  yielded approximately the band gap energy of the absorber. In conclusion, this method of extrapolating the open-circuit voltage is of no help in determining the major recombination path in the solar cell type investigated.

## 5.2 Damp-Heat Treatment of $\text{Cu}(\text{In,Ga})(\text{S,Se})_2$ -Based Solar Cells

In order to gain information on the potential major loss factors influenced by DH treatment, we applied the SCAPS program to investigate the influence of doping densities as well as concentrations of bulk and interface defect states on the open-circuit voltage and the band bending, guided by the experimental findings. Both, open-circuit voltage and band bending, are available experimentally, the latter being proportional to the activation energy of the defect state  $\beta$ . After 438h of DH exposure, we observed close to 20% loss in the open-circuit voltage  $V_{oc}$  (see Section 4.1) and a shift of the activation energy  $\Delta E$  of  $\beta$  from about 50meV to about 300meV (see Section 4.2.1). Using SCAPS, we compute which modifications of the sample definitions lead to electrical changes of a similar scale.

- reduction of the n-ZnO and i-ZnO doping densities by three orders of magnitude
  - can account for about a fifth of the  $V_{oc}$  loss and a clear increase of  $\Delta E$  (high i-ZnO doping)
  - for a low i-ZnO doping density, both parameters change only minimally
- a diminished concentration of interface defect states (by two orders of magnitude)
  - changes  $\Delta E$  drastically (low i-ZnO doping concentration)
  - for a high i-ZnO doping density, the changes happen on a much smaller scale.

In both cases the open-circuit voltage does not decrease.

- If both the doping density of the window layers and the concentration of interface states are reduced, then a major shift of  $\Delta E$  of the order of the experimentally observed values is seen
- a halved doping density of the absorber layer leads to a small reduction of  $V_{oc}$  and  $\Delta E$ , accounting for a tenth up to a fifth of the changes
- a high concentration of bulk defect states has the largest impact on the open-circuit voltage



- $\Delta E$  increases slightly for the case of acceptor-like defect states, but remains unaffected for recombination centers.

The change in the band diagram due to a combination of decreased doping densities of absorber and window, diminished concentration of interface defect states, and increased bulk trap concentration is shown in Figure 5.1.

Summarizing the results of our numerical simulations, the major contributor to the degradation of the open-circuit voltage is the increasing concentration of bulk defect states. The diminished band bending, represented by the increase of the activation energy of  $\beta$ , can be accounted for mainly by a diminishing concentration of interface states together with a decreasing doping density of the window layer.

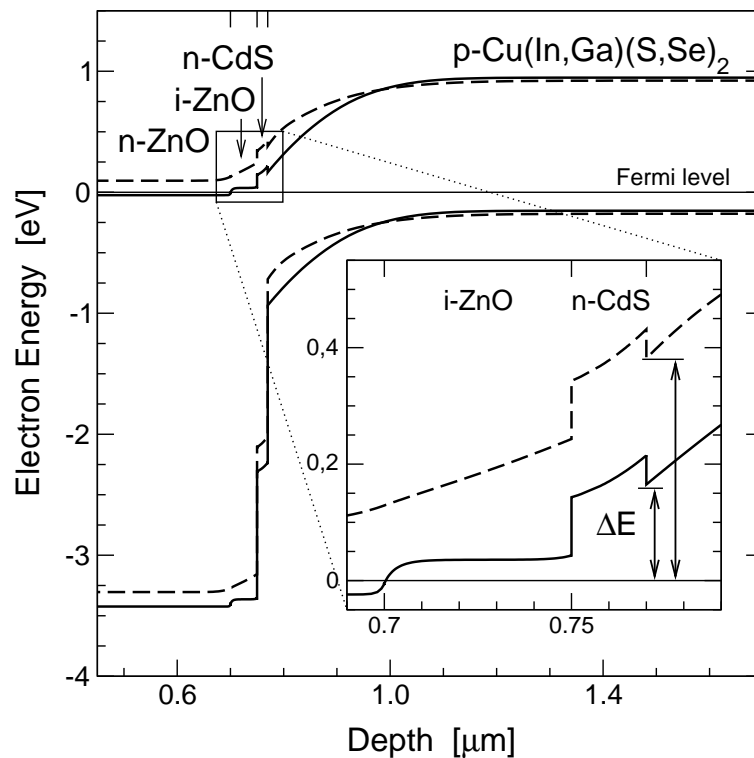


**Figure 5.1:** Band diagram of the n-ZnO/i-ZnO/CdS/Cu(In,Ga)(S,Se)<sub>2</sub> heterostructure at thermal equilibrium (with a blow-up focussing on the interfaces at the conduction-band edge), calculated using SCAPS [81]. The solid lines represent the conduction and valence band edges of a simulated reference cell. The dashed lines show a case, where the activation energy of a defect state at the CdS/Cu(In,Ga)(S,Se)<sub>2</sub> interface is increased due to changes at the interface (unpinning of the Fermi level) and bulk properties (increased concentration of a deep acceptor state in the absorber and decreased doping density in window and absorber).



## 6 Discussion

Three topics will be discussed in this section. The origin of the defect state  $\beta$  and its interpretation as interface defect state are critically examined (Section 6.1). The consequences for the influence of the CdS buffer layer on the contact formation and band bending are commented upon in Section 6.2. Finally, the influence of DH treatment on the electronic properties of the Cu(In,Ga)(S,Se)<sub>2</sub>-based solar cells are discussed (Section 6.3).

### 6.1 Origin of the Defect State $\beta$

The defect state  $\beta$  is observed in all Cu(In,Ga)(S,Se)<sub>2</sub>-based solar cells and Schottky contacts investigated in this work. Herberholz et al. [52] have interpreted  $\beta$  (called N1 therein) as interface defect state at the buffer/absorber interface. If this view indeed corresponds to the origin of  $\beta$ , it would render a direct determination of the changes of the heterostructure band bending possible. This section aims at the verification of the origin of the defect state  $\beta$ .

The state  $\beta$  is commonly observed in ZnO/CdS/Cu(In,Ga)(S,Se)<sub>2</sub> heterojunctions [71, 84, 85]. Herberholz et al. [52] reported  $\beta$  in ZnO/InS<sub>x</sub>/Cu(In,Ga)Se<sub>2</sub> heterostructures, we found it in ZnO/ZnSe/Cu(In,Ga)Se<sub>2</sub> samples and Cr/Cu(In,Ga)(S,Se)<sub>2</sub> Schottky diodes [41]. It is remarkable that the emission rate of  $\beta$  nearly coincides for as-grown heterostructure samples and as-grown Schottky diodes (see Figure 4.3). The experimental results provide evidence that the defect state  $\beta$  is affected (i.e., shifted) by the front contact (including the buffer layer), but located in the absorber layer.

The common origin of the different instances of the interface state  $\beta$  can be visualized using the Meyer-Neldel relation [84, 86], also called compensation law. It is given by

$$\nu_0 = \nu_{00} \exp\left(\frac{\Delta E}{E_c}\right), \quad (6.1)$$

where  $\nu_0$  denotes the attempt-to-escape frequency, which is the prefactor of the emission rate, see Equation (3.6). The prefactor  $\nu_{00}$  is approximately temperature independent. The characteristic energy  $E_c$  leads to the corresponding characteristic temperature  $T_c = E_c/k$ , defined by the intersection point of all curves in the Arrhenius plot which follow a distinct Meyer-Neldel relation. The interface state  $\beta$ , typically shifting to higher values of the activation energy and capture cross-section with time elapsed under DH conditions, obeys the Meyer-Neldel rule with  $E_c = 29\text{meV}$  (which is equivalent to about  $T_c = 336\text{K}$ ) and the prefactor  $\nu_{00} = 1.3 \times 10^7\text{Hz}$ , as can be seen in Figure 6.1. Even the shift of  $\beta$  due to different levels of reverse bias in case of a heterostructure sample exposed to DH treatment for 144h (where the Fermi-level pinning is lifted) follows the compensation law. The amplitude of the capacitance step related to  $\beta$  decreases proportional to the shift of the activation energy as

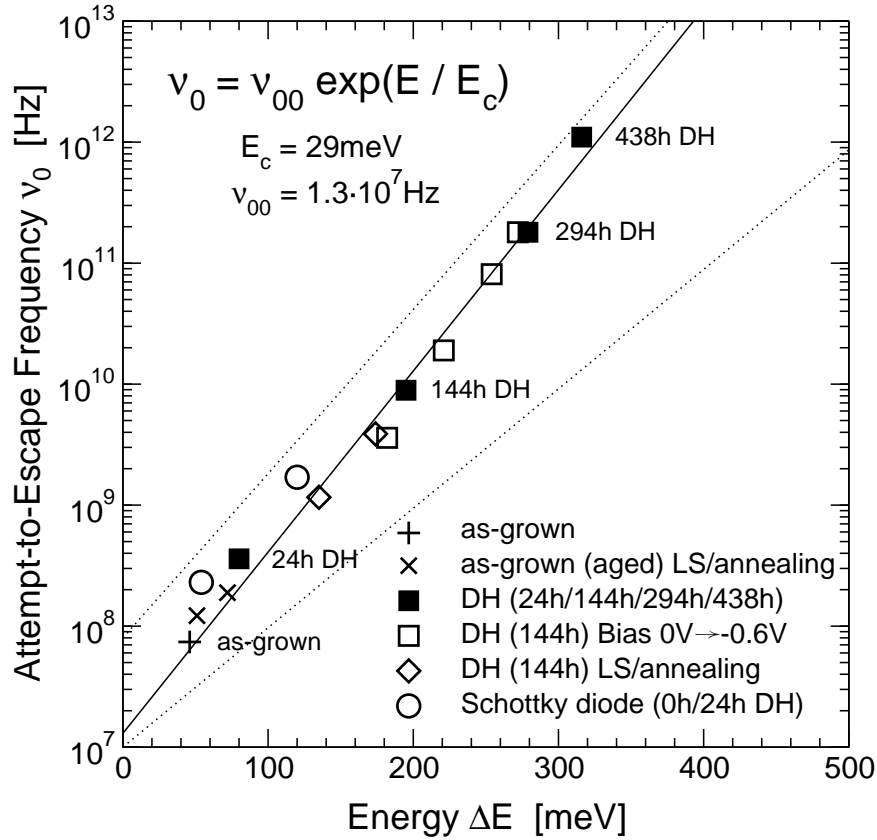


**Figure 6.1:** Meyer-Neldel rule of the activation energy  $\Delta E$  of the defect state  $\beta$  versus its attempt-to-escape frequency  $v_0$ . A good agreement of the different measurements with this distinct compensation law indicates a common origin of the different instances of the defect state  $\beta$ .

well [73]. These observations indicate that  $\beta$  is an energy-distributed defect state, possibly an interface defect state.

A dielectric relaxation due to a decreased response time of the free charge carriers is unlikely: defect states with emission rates faster than the dielectric relaxation time, like  $\alpha$  or  $\eta$ , can be observed in the same spectra as  $\beta$  in some samples. Igalson et al. [87] conclude from light-soaking experiments on Cu(In,Ga)Se<sub>2</sub>-based solar cells that  $\beta$  (called N1 therein) does not represent dielectric relaxation in the absorber layer. A dielectric relaxation in the CdS layer has been previously rejected by Niemegeers et al. [68], their estimation is supported by our observation of  $\beta$  independent of the front contact [41].

A location of  $\beta$  at internal Cu(In,Ga)(S,Se)<sub>2</sub> grain boundaries has to be considered. Grain boundaries are usually barriers for majority carriers [13, p. 134], i.e., the energy band is bent down at the grain boundaries in p-type material. Let us first discuss grain boundaries in parallel to the device interfaces. The activation energies of  $\beta$ , ranging from 50 to 300 meV, indicate that the Fermi level intersects the defect state relatively close to the corresponding band. If  $\beta$  were close to the valence band, the grain boundary would have to be situated deep in the absorber layer. Considering a Cu(In,Ga)(S,Se)<sub>2</sub> bulk Fermi level of 150–200 meV, the

small energies of about 50meV cannot be explained for the bending down of the energy band at the grain boundary. Thus, this case is unlikely, especially since  $\beta$  is a minority-carrier signal in DLTS, indicating that the Fermi level intersects the defect state close to the conduction band. The latter is only conceivable if  $\beta$  is located close to the type-inverted [21] Cu(In,Ga)(S,Se)<sub>2</sub> surface. Also, the DH-induced shift of  $\beta$  in part depends on the degradation of the ZnO window layer [73], a behavior which is expected if  $\beta$  is located close to the chalcopyrite surface. Thus, we rule out a location of  $\beta$  at an internal lateral grain boundary and conclude that  $\beta$  were located close to the Cu(In,Ga)(S,Se)<sub>2</sub>/front contact interface. Generally,  $\beta$  could originate from a longitudinal (perpendicular to the interfaces) grain boundary. The band bending in the absorber layer implies that the Fermi level intersects this (hypothetical) grain boundary state over the extent of the absorber layer, but the smallest energy difference (from the Cu(In,Ga)(S,Se)<sub>2</sub> front surface) would be the most favorable transition. However, usually voltage pulses *across* the grain boundary are necessary for detection with transient-capacitance methods [88], making a longitudinal grain boundary as the origin of  $\beta$  unlikely. Additionally, Scheer et al. [89, 90] report that grain boundaries in CuInSe<sub>2</sub> are not active for charge carrier recombination.

The interpretation of  $\beta$  as an energy distribution of interface defect states [52, 71] implies that its activation energy equals the difference in the conduction band minimum and the electron quasi Fermi level at the CdS/Cu(In,Ga)(S,Se)<sub>2</sub> interface. The assumed origin of this activation energy is shown in a blow-up of the corresponding band diagram in Figure 5.1. Igalson et al. [91] propose another explanation for the origin of the defect state  $\beta$ . They hold four discrete donor-like defect states in the absorber bulk (with activation energies of 80meV, 150meV, 350meV, and 570meV) responsible for the different instances of  $\beta$ . They also report on an additional influence of the junction electric field on the emission rates of those traps [91, 92].

The continuous shift of  $\beta$  induced by different treatments was principally responsible for the interpretation as interface defect state. The shift is mainly irreversible for exposure of the samples to the DH test [73] or air annealing at 240°C [52]. The changes induced by light soaking and helium gas annealing at about 65°C are reversible. We would like to note two findings indicating an energy distribution of states rather than discrete ones. First, the good agreement of the different measurements with one distinct Meyer-Neldel rule (see Figure 6.1) points to a common origin of the different instances of the defect state  $\beta$  [73]. Second, the height of the capacitance step changes continuously and is proportional to the activation energy [73], which is not expected for several discrete defect states.

With the help of DLTS, we have identified  $\beta$  as a minority-carrier signal [41], i.e., the width of the space charge region diminishes directly after having applied the filling pulse. If  $\beta$  were a bulk trap, it would probably be a donor-like defect state. A prerequisite to detect such a shallow bulk minority-carrier trap — the activation energy of  $\beta$  for as-grown samples amounts to about 50meV — is a large band bending close to the interface between the front contact and the absorber, confining the possible spatial location of the detection of the defect state to the Cu(In,Ga)(S,Se)<sub>2</sub> surface. We have already discussed in Section 3.2.2 that bulk minority-carrier defect states can be detected in Cu(In,Ga)(S,Se)<sub>2</sub>-based heterojunctions and Schottky contacts even without minority-carrier injection.

The Arrhenius representation of the temperature-dependent emission rates of  $\beta$ , plotted in in Figure 4.3, is a slightly bent curve. This nonlinearity can have several reasons, e.g., a tunneling contribution due to the junction electric field [92], a capture of charge carriers

in the space charge region due to high leakage currents [65], or because the small-signal approximation (amplitude of the alternating voltage for capacitance measurement has to be much smaller than the thermal voltage  $kT/e$ ) is invalid at low temperatures [93]. A final classification is not possible yet.

The shift of the temperature-dependent emission rates and capacitance step heights of the defect state  $\beta$  is continuous. Therefore, we consider the interpretation of  $\beta$  as energy-distributed defect state in the  $\text{Cu}(\text{In,Ga})(\text{S,Se})_2$  surface region to be more likely than the proposition of Igalson et al. [91]. However, we can draw conclusions about the band bending of the junction using either model. With the common interpretation of  $\beta$  as an interface defect state, the information on the band bending is directly obtained by the measured activation energy. In the Igalson model, the detection of a minority-carrier defect state located in the absorber layer with activation energies as low as 80meV is only possible for the electron quasi Fermi level being very close to the conduction band. We conclude that the detection of  $\beta$  in as-grown  $\text{Cu}(\text{In,Ga})(\text{S,Se})_2$ -based heterojunctions and Schottky contacts signifies a strong band bending.

## 6.2 Contact Formation

The process of contact formation and its consequences for the band bending of the  $\text{Cu}(\text{In,Ga})(\text{S,Se})_2$ -based heterojunction are not fully understood yet. A model proposed by Rau et al. [12] explains the relatively high band bending of heterojunction devices by an absorber surface passivation due to the subsequent CdS bath deposition. We demonstrate that the band bending within the  $\text{Cu}(\text{In,Ga})(\text{S,Se})_2$  layer, reported in the literature to become minimal after air exposure, is restored after the formation of either a Schottky contact or a heterojunction. The above phenomenon turns out to be independent of a surface passivation due to the CdS bath deposition.

$\text{Cu}(\text{In,Ga})(\text{S,Se})_2$  films exposed to ambient air display a relatively small band bending, as reported by Weinhardt et al. [25] who measured a Fermi-level position (relative to the conduction band minimum) of 0.5eV via applying inverse photoemission spectroscopy. In-vacuo as-grown  $\text{Cu}(\text{In,Ga})\text{Se}_2$  surfaces, however, show a type inversion [21], i.e., the Fermi level is very close to the conduction band [24]. The impact of ambient air on the band bending of  $\text{Cu}(\text{In,Ga})\text{Se}_2$  films has been measured directly by Rau et al. [12]. They observed a 200meV decrease of the band bending using in-situ ultraviolet photoelectron spectroscopy after contact with ambient air compared to the in-vacuo result. Devices finished after an air exposure of the absorber layer, however, show a high band bending again [73]. In order to explain such a phenomenon, Rau et al. [12] proposed that the CdS bath deposition is responsible for a reintroduction of positive surface charges and a restoration of the band bending to the state before the air exposure.

Our capacitance measurements demonstrate a high band bending for both,  $\text{ZnO}/\text{CdS}/\text{Cu}(\text{In,Ga})(\text{S,Se})_2$  heterojunctions and  $\text{Cr}/\text{Cu}(\text{In,Ga})(\text{S,Se})_2$  Schottky contacts, even though the respective absorber layers were exposed to ambient air during processing. Thus, the restoration of the band bending is independent of the CdS bath deposition, dissenting the model from Rau et al. [12]. The mechanism being responsible for such behavior is still unknown. The possible explanation would be a Fermi-level pinning by a high concentration of interface defect states only after contact formation, independent

of the contact layer applied, i.e., a reorganization of the chalcopyrite surface due to the junction built-in electric field. Such an effect could result from the field-induced migration of Cu [12, 24].

A good performance of other buffer layers as alternatives [19] for CdS supports our findings in suggesting that CdS plays no exceptional role in the contact formation. However, the one argument in favor of CdS as buffer layer in heterojunction solar cells is its relatively good DH stability [20].

## 6.3 On the Influence of the Damp-Heat Treatment

The influence of water vapor and oxygen on the charge transport properties of the heterostructure cells is the focus of this thesis. Oxygen-related phenomena have been discussed in literature for more than a decade [94], and extensive work covering oxygenation [12] and related topics [95] is available. The impact of water vapor on the cell characteristics goes beyond the magnitude of the influence of oxygen [8], even though both effects are closely related to each other. Changes of the transport properties of CuInSe<sub>2</sub> based thin-film solar cells due to exposure to DH have recently been investigated with regard to modifications in the window [8, 96, 97] and absorber layer [41, 67, 71, 72, 73]. So far, the impact of stress tests on the back contact of the solar cells has been described only qualitatively [96, 97]. A fraction of the DH induced changes is reversible under illumination (referred to as light soaking). Such metastability most likely originates from the absorber layer [8]. In this context (also concerning the differences of DH exposure to oxygenation [12]), it should be mentioned that the effect of dry air annealing (85°C, 2000h) on the electronic properties is much smaller than that of DH exposure [8].

The experimental findings presented in this thesis indicate that all layers of the Cu(In,Ga)(S,Se)<sub>2</sub> based heterostructure cells contribute to the DH induced changes of the fill factor and open-circuit voltage. We discuss the different layers successively, also giving account of the findings of other authors in the literature.

### 6.3.1 Window Layer

The front electrode commonly consists of an n-ZnO layer, an undoped i-ZnO layer, and a CdS buffer layer, the latter being in direct contact with the absorber. Experimental analysis of the surface morphology of DH tested Cu(In,Ga)Se<sub>2</sub> based heterostructure cells unveils some deterioration of the window layer due to microdefects of sizes ranging from 5 to 40 μm, which are located directly at the surface [98]. The DH exposure of ZnO layers on glass or Si substrates has been demonstrated to result in an increasing sheet resistance [8, 96, 97]. The degree of degradation is enhanced by the CdS layer located between ZnO and substrate, and is proportional to the thickness of the CdS layer [96, 97]. The increase in sheet resistance observed after 1000h DH testing is found to be in the range between two and three. Wennerberg et al. [97] attribute these changes to a decreasing carrier concentration in the ZnO layers. The increased sheet resistance of the ZnO window can account for only a small fraction of the fill factor losses [97, 99]. For modules, usually produced without a metal grid deposited on top of the window layer, the increase in sheet resistance has a considerably larger effect on the overall performance [100].

Our own findings verify the small significance of the sheet resistance of the window layer on the performance of laboratory-scale samples: comparing test cells that were DH treated as fully processed device with the sets of samples where the process sequence was interrupted for a DH exposure after the absorber RTP, the CdS deposition, or the i-ZnO sputter process, respectively, it becomes clear that the degradation of the window layer can be made responsible only for a small share of the total power loss [73].

### 6.3.2 Window/Absorber Interface

Lang et al. [101] point out that the surface of the absorber does not have the form of just a monolayer of atoms, but rather is a transition region to the bulk semiconductor. Taking advantage of capacitance spectroscopy and DLTS, it seems to be impossible to distinguish between a certain kind of defect located directly at the surface layer or inside a thin interface region. Such a problem remains unsolved for the origin of the defect state  $\beta$  found in CuInSe<sub>2</sub> based solar cells, where the existence of an ordered vacancy or defect compound (OVC/ODC) of a few nanometers thickness has been reported [68].

Our capacitance spectroscopy measurements clearly show that the electrical properties of the interface region are modified by heat and humidity treatment. However, the shift of the interface defect state  $\beta$ , observed after DH exposure [41, 71, 72] and air annealing [52], does not only stem from changes of the interface, but is also influenced by the window and absorber bulk regions (doping concentration, defect state concentration) as well. Thus, the band bending of the heterojunction and the type inversion at the absorber surface are diminished. Focussing on the results obtained for the interface, we find that the Fermi-level pinning of as-grown cells is lifted for the case of complete devices [71] (see Figure 4.5), but remains unchanged when only the absorber layer was exposed to DH and the window layer deposited afterwards [73]. Consequently, the density of interface defect states is diminished due to the DH treatment of n-ZnO/i-ZnO/CdS/Cu(In,Ga)(S,Se)<sub>2</sub>/Mo solar cells.

The defect state  $\theta$ , being observed after DH treatment (see Figure 4.2(b)), is probably located at the window/buffer interface or an internal grain boundary. We were not able to verify the spatial location and, thus, cannot judge the relevance of this defect state for the electrical changes of the DH treated samples.

Chemical modifications of the interface region due to heat and humidity have been observed as well. Weinhardt et al. [25] have performed photoemission and X-ray emission spectroscopy experiments on Cu(In,Ga)(S,Se)<sub>2</sub>-based heterostructures. They report on a DH induced oxidation of S atoms at the ZnO/CdS interface or at the ZnO/Cu(In,Ga)(S,Se)<sub>2</sub> interface, but do not observe oxidation at the CdS/Cu(In,Ga)(S,Se)<sub>2</sub> interface. Karg et al. [8] point out that the oxygen content of the cells, normally about one per mille of the amount of CuInSe<sub>2</sub>, increases up to one order of magnitude due to DH exposure. The oxygen accumulates particularly at the buffer/absorber interface and the absorber/Mo interface. Such an effect is reported to be most pronounced for the case of Na doped films.

On base of the current data, we cannot relate our electronic measurements to the observation of chemical modifications by other groups. The CdS/Cu(In,Ga)(S,Se)<sub>2</sub> interface region degrades due to DH exposure and might be responsible for a fraction of the solar cell degradation, even though the numerical simulations do not suggest an influence on the degradation process. However, one should bear in mind that many simulation parameters are based on estimates only. We are not able to distinguish between a dominant recombination at the



buffer/absorber interface or in the absorber bulk by experimental means.

### 6.3.3 Absorber Layer

Some of the bulk defect states detected in  $\text{Cu}(\text{In,Ga})(\text{S,Se})_2$  based heterojunction cells are related to the DH induced degradation. We observe the acceptor-like defect states  $\zeta$  and  $\gamma$  as well as the recombination center  $\varepsilon$ . The former one can be found after 144h of DH treatment, but is present in relatively low concentrations only.  $\gamma$  and  $\varepsilon$  can be observed clearly in as-grown samples, but their concentration is diminished due to the exposure to DH conditions. However, we believe that the concentrations determined are distorted by the influence of leakage currents [65], and by a superposition with another defect state in the case of  $\gamma$ . Additionally, the corresponding capacitance transients are non-exponential, making the standard method for evaluation of the defect concentration inaccurate [11]. This case usually takes place for high defect concentrations (order of a tenth of the doping density) and especially for highly compensated semiconductors like  $\text{Cu}(\text{In,Ga})(\text{S,Se})_2$  [102], as the band bending in the depletion region is significantly changed when charge carriers are emitted from the deep traps [103]. Thus, we are not able to quantitatively describe the DH induced changes of the defect spectra.

Other groups have reported the observation of defect states related to the DH test as well. Schmidt et al. [72] measured an acceptor-like defect state called N2, which is present in their as-grown co-evaporated samples in a relatively high concentration, as it can be measured with admittance spectroscopy. They correlated the concentration of this defect state (estimated with a calculation done by Walter et al. [50] based on their admittance data) with the open-circuit voltage of their devices. N2 is presumably identical to  $\zeta$ , even though its significance for the electrical characteristics seems to be quite different. Igalson et al. [67] observed N2 and a donor-like defect state N3 (with emission rates comparable to  $\varepsilon$ ) only after DH treatment using DLTS, but did not determine the defect concentration.

A pronounced current–voltage hysteresis, observed only after DH exposure of heterojunction samples and Schottky contacts, indicates a trapping mechanism in the absorber layer, i.e., an increasing concentration of deep traps. Also, within the numerical simulations, only an increasing concentration of deep defect states in the absorber layer can account for a major fraction of the losses of the open-circuit voltage (see Figure 6.2). A decreasing absorber doping density due to DH exposure is equivalent to a reduced compensation, i.e., a net decrease of acceptor states — which, of course, can be achieved by an increasing concentration of donor-like states as well. However, the experimentally observed decreasing concentration of acceptor-like defect states can lead to a reduced compensation, but cannot account for the hysteresis. Thus, the detailed changes of the deep traps due to DH treatment as well as the resulting electronic modifications are still not clarified.

Let us finally discuss the relation of the DH exposure and air annealing (oxygenation [12, 94]) phenomena to each other. The experimental difference is that DH testing is performed at a relatively low ambient temperature (85°C) combined with humidity treatment (i.e., including hydrogen), whereas air (or oxygen) annealing happens at temperatures of above 200°C without being subject to water vapor. The two major effects of oxygenation are a passivation of Se vacancies at the CdS/chalcopyrite interface and Cu migration into the absorber bulk [12]. We emphasize that both explanations are only model pictures proposed to support various experimental findings, but have been observed directly neither for air an-

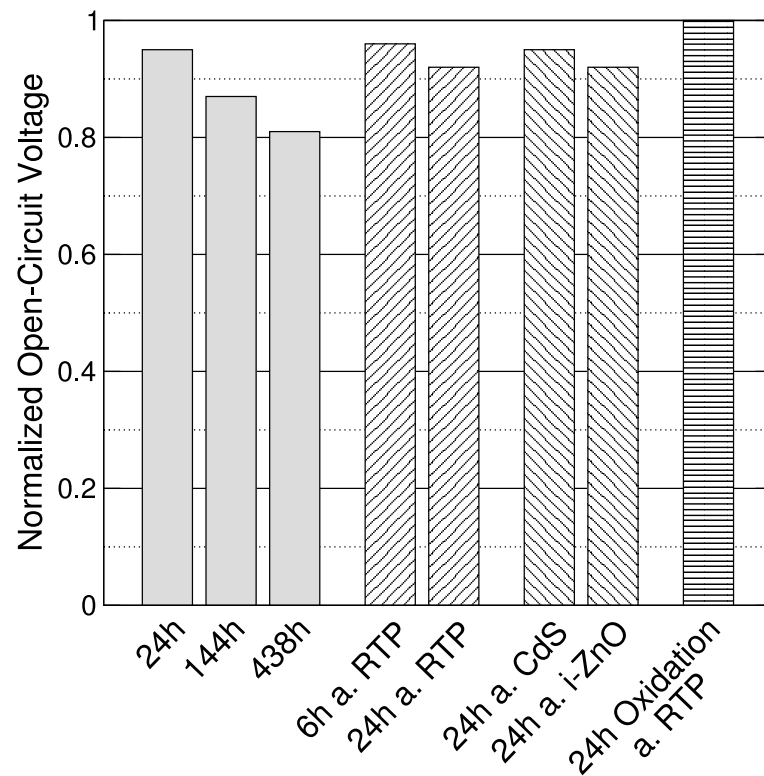


**Figure 6.2:** Histogram of the normalized open-circuit voltage of different sets of DH treated samples. For some sets of samples, the processing sequence was interrupted for a DH treatment after the deposition of a certain layer. The cell process was continued afterwards. The corresponding samples are denoted as, e.g., 6h a. RTP, meaning 6h of DH exposure after deposition of the absorber layer. Instead of DH treatment, one set of samples was annealed in dry air atmosphere (85°C, 24h) after RTP.

nealing nor for DH treatment. However, oxygen might play an important role for the effects of DH exposure, as the amount of oxygen present in Na containing absorber layers increases by about one order of magnitude due to accelerated lifetime tests [8]. The role of hydrogen in Cu(In,Ga)(S,Se)<sub>2</sub>-based solar cells is still unclear, even though it has been found in high concentrations of  $10^{18}\text{cm}^{-3}$  in as-grown samples [104]. To our knowledge, the hydrogen concentration in dependence on the DH treatment has not been investigated yet. The similar results of the DH and annealing experiments, i.e., the shift of the interface defect state  $\beta$  and a decreased net doping density of the absorber, indicate a common origin for some of the underlying modifications, even though the correlation of the chemical changes with the electronic properties remains unclear.

### 6.3.4 Back Contact

The Mo back contact undergoes an oxidation process due to DH exposure [97], but such degradation becomes electrically significant only if the module interconnections are destroyed [96]. Our electrical measurements indicate that no additional electronic barrier exists

evolving due to the DH treatment of complete heterostructure samples with durations of up to 438h, i.e., the interface between the bulk absorber and the back contact remains ohmic.



## 7 Conclusions

The electronic characteristics of as-grown and damp-heat treated ZnO/CdS/Cu(In,Ga)(S,Se)<sub>2</sub>/Mo heterojunction solar cells and Cr/Cu(In,Ga)(S,Se)<sub>2</sub>/Mo Schottky contacts have been investigated using current–voltage and capacitance–voltage measurements, admittance spectroscopy, and deep-level transient spectroscopy.

A pronounced defect state with a continuously shifting activation energy depending on the sample treatment presumably originates from an energy distribution of defect states located at the Cu(In,Ga)(S,Se)<sub>2</sub> surface. The activation energy of this energy distribution indicates the degree of band bending, which is relatively small after air exposure, but increases considerably after the formation of a Schottky contact or a heterojunction. The increase of the band bending after the contact formation is independent of the presence of the CdS buffer layer.

The electronic effects of the damp-heat treatment at 85°C ambient temperature and 85% relative humidity on ZnO/CdS/Cu(In,Ga)(S,Se)<sub>2</sub>/Mo heterojunction solar cells have been investigated. We observed a reduced net doping density in the chalcopyrite absorber layer. Three absorber bulk traps with non-exponential capacitance transients were detected, two acceptor-like defect states and a recombination center. We were not able to determine the absolute trap concentrations, and make superposition effects and the influence of leakage currents responsible for distorted capacitance transient amplitudes. However, the observation of a hysteresis in the current–voltage characteristics of damp-heat treated heterojunctions and Schottky contacts aims at an increased concentration of traps in the absorber layer. The Fermi-level pinning at the buffer/chalcopyrite interface, maintaining a high band bending in as-grown cells, is lifted due to the damp-heat exposure. The sheet resistance of the window layer increases. The combination of these effects leads to a reduction of the band bending and a diminished open-circuit voltage in the damp-heat treated solar cells.

The influence of the damp-heat treatment on the electronic properties of Cu(In,Ga)(S,Se)<sub>2</sub>-based heterojunction solar cells is well described (in part owing to the present work), but the underlying mechanisms are still poorly understood — this is also the case for many other aspects of this complex material system. One major problem is the inadequate correlation of the results of complementary measurement techniques, which is essential for the advance of the insight into the physical origin of the damp-heat induced degradation.



# Danksagung

Ich möchte mich an dieser Stelle bei all denjenigen bedanken, die maßgeblich zum Gelingen dieser Arbeit beigetragen haben. Mein Dank gilt

- Prof. Dr. Jürgen Parisi, welcher mir die Durchführung dieser Arbeit ermöglicht hat, für die kontinuierliche Unterstützung
- Dr. Vladimir Dyakonov für die Betreuung
- meinem ehemaligen Diplomanden Arne Wessel für Diskussionen und vieles mehr
- meinem ehemaligen Diplomanden Marco Munzel. Laß uns mal wieder Eis machen
- meiner Nachfolgerin Verena Mertens, u.a. für das Korrekturlesen dieser Arbeit
- Holger Koch und Hans Holtorf, für die praktische und moralische Unterstützung
- Dr. Achim Kittel für zahlreiche hilfreiche Diskussionen
- Elizabeth von Hauff für das Korrekturlesen dieser Arbeit. Alle noch vorhandenen Fehler sind meine eigenen;)
- Markus Backes und Tobias Letz für vieles
- meinen Kollegen und Kolleginnen in der Photovoltaik-Gruppe und der EHF für das freundschaftliche und angenehme Arbeitsklima
- Prof. Dr. Gottfried Bauer für interessante Gespräche
- Karsten Bothe (ISFH) für interessante Diskussionen mit und ohne Wein
- Marc Köntges und Stephan Ulrich (ISFH) für Ideenaustausch und Unterstützung
- Dr. Uwe Rau (Uni Stuttgart) für fachliche Diskussionen
- Dr. Malgorzata Igalson (Uni Warschau) für ihren Besuch in Oldenburg, welcher von zahlreichen Informationen zu DLTS und interessanten Unterhaltungen geprägt war
- Dr. Jörg Palm (Shell Solar, München) für die gute Zusammenarbeit und viele interessante und oft kontroverse Diskussionen
- Dr. Riedl, Dr. Zweigart und Dr. Karg für die gute Zusammenarbeit und Bereitstellung der Proben (Shell Solar, München)
- den Projektpartnern von der Universität Würzburg und dem Hahn-Meitner Institut Berlin
- der Siemens AG für die finanzielle Unterstützung
- nicht zuletzt meinen Eltern, meiner Großmutter und meiner Freundin Antje für moralische Unterstützung und vieles mehr. Aber das sage ich ihnen lieber persönlich;)





# Bibliography

- [1] L. D. Partain, P. S. McLeod, J. A. Duisman, T. M. Peterson, R. E. Weiss, and C. S. Dean. Degradation of  $\text{Cu}_x\text{S}/\text{CdS}$  in hot, moist air: experiment and theory. In *Proceedings of the 16th IEEE Photovoltaic Specialists Conference, San Diego, USA*, page 883, 1982.
- [2] R. A. Mickelsen and W. S. Chen. Development of a 9.4% efficient thin-film  $\text{CuInSe}_2/\text{CdS}$  solar cell. In *Proceedings of the 15th IEEE Photovoltaic Specialists Conference, Kissimmee, USA*, page 800, 1981.
- [3] K. W. Mitchell and H. I. Liu. Device analysis of  $\text{CuInSe}_2$  solar cells. In *Proceedings of the 20th IEEE Photovoltaic Specialists Conference, Las Vegas, USA*, page 1461, 1988.
- [4] M. A. Contreras, B. Egaas, K. Ramanathan, J. Hiltner, A. Swartzlander, F. Hasoon, and R. Noufi. Progress towards 20% efficiency in  $\text{Cu}(\text{In,Ga})\text{Se}_2$  polycrystalline thin-film solar cells. *Prog. Photovolt.*, 7:311, 1999.
- [5] J. Palm, V. Probst, R. Tölle, T. P. Niesen, S. Visbeck, O. Hernandez, M. Wendl, H. Vogt, H. Calwer, B. Freienstein, and F. Karg. CIS module pilot processing applying concurrent rapid selenization and sulfurization of large area thin film precursors. *Thin Solid Films*, 2002. In press.
- [6] M. Powalla and B. Dimmler. Pilot line production of CIGS modules: First experience of processing and further developments. In T. Anderson, editor, *Proceedings of the 29th IEEE Photovoltaic Specialists Conference, New Orleans, USA*, IEEE, New York, 2002. In press.
- [7] V. Probst, W. Stetter, W. Riedl, H. Vogt, M. Wendl, H. Calwer, S. Zweigart, K.-D. Ufert, B. Freienstein, H. Cerva, and F. H. Karg. Rapid CIS-process for high efficiency PV-modules: development towards large area processing. *Thin Solid Films*, 387:262, 2001.
- [8] F. Karg, H. Calwer, J. Rimmasch, V. Probst, W. Riedl, W. Stetter, H. Vogt, and M. Lampert. Development of stable thin film solar modules based on  $\text{CuInSe}_2$ . In R. D. Tomlinson, A. E. Hill, and R. D. Pilkington, editors, *Proceedings of the 11th International Conference on Ternary and Multinary Compounds, Salford, UK*, page 909, Institute of Physics, Bristol, 1998.
- [9] D. E. Tarrant and R. R. Gay. Thin-film photovoltaic partnership — CIS-based thin film PV technology. Final tech. report, 9/1995 – 12/1998, NREL, October 1999.

- [10] D. L. Losee. Admittance spectroscopy of impurity levels in Schottky barriers. *J. Appl. Phys.*, 46:2204, 1975.
- [11] D. V. Lang. Deep-level transient spectroscopy: A new method to characterize traps in semiconductors. *J. Appl. Phys.*, 45:3023, 1974.
- [12] U. Rau, D. Braunger, R. Herberholz, H. W. Schock, J.-F. Guillemoles, L. Kronik, and D. Cahen. Oxygenation and air-annealing effects on the electronic properties of Cu(In,Ga)Se<sub>2</sub> films and devices. *J. Appl. Phys.*, 86:497, 1999.
- [13] H.-J. Lewerenz and H. Jungblut. *Photovoltaik: Grundlagen und Anwendungen*. Springer, Berlin, 1995.
- [14] U. Rau and M. Schmidt. Electronic properties of ZnO/CdS/Cu(In,Ga)Se<sub>2</sub> solar cells — aspects of heterojunction formation. *Thin Solid Films*, 387:141, 2001.
- [15] J. Santamaria, G. Gonzalez, E. Iborra, I. Martil, and F. Sanchez-Quesada. Role of deep levels and interface states in the capacitance characteristics of all-sputtered CuInSe<sub>2</sub>/CdS solar cell heterojunctions. *J. Appl. Phys.*, 65:3236, 1989.
- [16] T. Nehami, Y. Hashimoto, and S. Nishiwaki. Cu(In,Ga)Se<sub>2</sub> thin-film solar cells with an efficiency of 18%. *Sol. Ener. Mat. Sol. Cells*, 67:331, 2001.
- [17] F. Engelhardt, L. Bornemann, M. Köntges, T. Meyer, J. Parisi, E. Pschorr-Schoberer, B. Hahn, W. Gebhardt, W. Riedl, and U. Rau. Cu(In,Ga)Se<sub>2</sub> solar cells with a ZnSe buffer layer: interface characterization by quantum efficiency measurements. *Prog. Photovolt.*, 7:423, 1999.
- [18] J.-B. Yoo, A. L. Fahrenbruch, and R. H. Bube. Effects of a thin intermediate zinc selenide layer on the properties of CuInSe<sub>2</sub> solar cells. *Sol. Cells*, 31:171, 1991.
- [19] T. Nakada, M. Mizutani, Y. Hagiwari, and A. Kunioka. High-efficiency Cu(In,Ga)Se<sub>2</sub> thin-film solar cells with a CBD-ZnS buffer layer. *Sol. Ener. Mat. Sol. Cells*, 67:255, 2001.
- [20] M. Bär, C.-H. Fischer, H.-J. Muffler, B. Leupolt, T. P. Niesen, F. Karg, and M. C. Lux-Steiner. High efficiency chalcopyrite solar cells with ILGAR-ZnO WEL — device characteristics subject to the WEL composition. In *Proceedings of the 29th IEEE Photovoltaic Specialists Conference, New Orleans, USA*, IEEE, New York, 2002. In press.
- [21] D. Schmid, M. Ruckh, and H. W. Schock. A comprehensive characterization of the interface in Mo/CIS/CdS/ZnO solar cell structures. *Sol. Ener. Mat. Sol. Cells*, 41/42: 281, 1996.
- [22] C. Heske, D. Eich, R. Fink, E. Umbach, T. van Buuren, L. J. Terminello, S. Kakar, M. M. Grush, T. A. Calcott, F. J. Himpsel, D. L. Ederer, R. C. C. Perera, W. Riedl, and F. Karg. Observation of intermixing at the buried CdS/Cu(In,Ga)Se<sub>2</sub> thin film solar cell heterojunction. *Appl. Phys. Lett.*, 74:1451–1453, 1999.

- [23] I. Luck, U. Störkel, W. Bohne, A. Ennaoui, M. Schmidt, H.-W. Schock, and D. Bräunig. Influence of buffer layer and TCO deposition on the bulk properties of chalcopyrites. *Thin Solid Films*, 387:100, 2001.
- [24] A. Klein and W. Jaegermann. Fermi-level-dependent defect formation in Cu-chalcopyrite semiconductors. *Appl. Phys. Lett.*, 74:2283, 1999.
- [25] L. Weinhardt, M. Morkel, Th. Gleim, S. Zweigart, T. P. Niesen, F. Karg, C. Heske, and E. Umbach. Band alignment at the CdS/CuIn(S,Se)<sub>2</sub> heterojunction in thin film solar cells. In B. McNelis, W. Palz, H. A. Ossenbrink, and P. Helm, editors, *Proceedings of the 17th European Photovoltaic Solar Energy Conference, Munich, Germany*, page 1261, WIP, München, 2002.
- [26] I. L. Eisgruber, J. E. Granata, J. R. Sites, J. Hou, and J. Kessler. Blue-photon modification of nonstandard diode barrier in CuInSe<sub>2</sub> solar cells. *Sol. Ener. Mat. Sol. Cells*, 53:367, 1998.
- [27] M. Munzel, C. Deibel, V. Dyakonov, J. Parisi, W. Riedl, and F. Karg. Electrical characterization of defects in Cu(In,Ga)Se<sub>2</sub> solar cells containing a ZnSe or a CdS buffer layer. *Thin Solid Films*, 387:231, 2001.
- [28] M. Köntges, R. Reineke-Koch, P. Nollet, J. Beier, R. Schäffler, and J. Parisi. Light induced changes in the electrical behaviour of CdTe and Cu(In,Ga)Se<sub>2</sub> solar cells. *Thin Solid Films*, 403/404:280, 2002.
- [29] J. H. Schön, E. Arushanov, C. Kloc, and E. Bucher. Electrical and photoluminescence properties of CuInSe<sub>2</sub> single crystals. *J. Appl. Phys.*, 81:6205, 1997.
- [30] R. Herberholz, U. Rau, H. W. Schock, T. Haalboom, T. Gödecke, F. Ernst, C. Beilharz, K. W. Benz, and D. Cahen. Phase segregation, Cu migration and junction formation in Cu(In,Ga)Se<sub>2</sub>. *Europ. Phys. J. Appl. Phys.*, 6:131, 1999.
- [31] R. Klenk, T. Walter, H. W. Schock, and D. Cahen. A model for the successful growth of polycrystalline films of CuInSe<sub>2</sub> by multisource physical vacuum evaporation. *Adv. Materials*, 5:114, 1993.
- [32] S. B. Zhang, S.-H. Wei, A. Zunger, and H. Katayama-Yoshida. Defect physics of the CuInSe<sub>2</sub> chalcopyrite semiconductor. *Phys. Rev. B*, 57:9642, 1998.
- [33] L. Stolt, J. Hedström, J. Kessler, M. Ruckh, K. O. Velthaus, and H. W. Schock. ZnO/CdS/CuInSe<sub>2</sub> thin-film solar cells with improved performance. *Appl. Phys. Lett.*, 62:597, 1993.
- [34] V. Probst, F. Karg, J. Rimmasch, W. Riedl, W. Stetter, H. Harms, and O. Eibl. Advanced stacked elemental layer process for Cu(In,Ga)Se<sub>2</sub> thin film photovoltaic devices. In *Proceedings of the Materials Research Society Symposium*, volume 426, page 165, 1996.

- [35] U. Rau, M. Schmitt, D. Hilburger, F. Engelhardt, O. Seifert, and J. Parisi. Influence of Na and S incorporation on the electronic transport properties of Cu(In,Ga)Se<sub>2</sub> solar cells. In *Proceedings of the 25th IEEE Photovoltaic Specialists Conference, Washington, USA*, May 1996.
- [36] S.-H. Wei, S. B. Zhang, and A. Zunger. Effects of Na on the electrical and structural properties of CuInSe<sub>2</sub>. *J. Appl. Phys.*, 85:7214, 1999.
- [37] C. Heske, D. Eich, R. Fink, E. Umbach, S. Kakar, T. van Buuren, C. Bostedt, L. J. Terminello, M. M. Grush, T. A. Calcott, F. J. Himpsel, D. L. Ederer, R. C. C. Perera, W. Riedl, and F. Karg. Localization of Na impurities at the buried CdS/Cu(In,Ga)Se<sub>2</sub> heterojunction. *Appl. Phys. Lett.*, 75:2082, 1999.
- [38] A. M. Gabor, J. R. Tuttle, D. S. Albin, M. A. Contreras, and R. Noufi. High-efficiency CuIn<sub>x</sub>Ga<sub>1-x</sub>Se<sub>2</sub> solar cells made from (In<sub>x</sub>Ga<sub>1-x</sub>)<sub>2</sub>Se<sub>3</sub> precursor films. *Appl. Phys. Lett.*, 65:198, 1994.
- [39] V. Probst, W. Stetter, J. Palm, S. Zweigart, M. Wendl, H. Vogt, K.-D. Ufert, H. Calwer, B. Freienstein, and F. H. Karg. Large area CIS formation by rapid thermal processing of stacked elemental layer. In B. McNelis, W. Palz, H. A. Ossenbrink, and P. Helm, editors, *Proceedings of the 17th European Photovoltaic Solar Energy Conference, Munich, Germany*, page 262, WIP, München, 2002.
- [40] W. N. Shafarman and J. E. Philips. Direct current-voltage measurements of the Mo/CuInSe<sub>2</sub> contact on operating solar cells. In *Proceedings of the 25th IEEE Photovoltaic Specialists Conference, Washington, USA*, 1996.
- [41] C. Deibel, V. Dyakonov, J. Parisi, J. Palm, and F. Karg. Damp-heat treatment of Cu(In,Ga)(S,Se)<sub>2</sub> solar cells. In *Proceedings of the 29th IEEE Photovoltaic Specialists Conference, New Orleans, USA*, IEEE, New York, 2002. In press.
- [42] P. Blood and J. W. Orton. *The electrical characterization of semiconductors: majority carriers and electron states*. Academic Press, New York, 1992.
- [43] M.-F. Li. *Modern semiconductor quantum physics*. World Scientific, Singapore, 1994.
- [44] W. Shockley and W. T. Read, Jr. Statistics of the recombination of holes and electrons. *Phys. Rev.*, 87:835, 1952.
- [45] R. N. Hall. Electron-hole recombination in germanium. *Phys. Rev.*, 87:387, 1952.
- [46] C. H. Henry and D. V. Lang. Nonradiative capture and recombination by multiphonon emission ins GaAs and GaP. *Phys. Rev. B*, 15:989, 1977.
- [47] A. Schenk. A model for the field and temperature dependence of Shockley-Read-Hall lifetimes in silicon. *Solid State Electron.*, 35:1585, 1992.
- [48] G. A. M. Hurkx, D. B. M. Klaassen, and M. P. G. Knuvers. A new recombination model for device simulation including tunneling. *IEEE Transactions on Electron Devices*, 39:331, 1992.

- [49] D. L. Losee. Admittance spectroscopy of deep impurity levels: ZnTe Schottky barriers. *Appl. Phys. Lett.*, 21:54, 1972.
- [50] T. Walter, R. Herberholz, C. Müller, and H. W. Schock. Determination of defect distributions from admittance measurements and application to Cu(In,Ga)Se<sub>2</sub> based heterojunctions. *J. Appl. Phys.*, 80:4411, 1996.
- [51] E. H. Nicollian and A. Goetzberger. MOS conductance technique for measuring surface state parameters. *Appl. Phys. Lett.*, 7:216, 1965.
- [52] R. Herberholz, M. Igalson, and H. W. Schock. Distinction between bulk and interface states in CuInSe<sub>2</sub>/CdS/ZnO by space charge spectroscopy. *J. Appl. Phys.*, 83:318, 1998.
- [53] J. H. Werner, K. Ploog, and H. J. Queisser. Interface-state measurements at Schottky contacts: A new admittance technique. *Phys. Rev. Lett.*, 57:1080, 1986.
- [54] C. T. Sah, L. Forbes, L. L. Rosier, and A. F. Tasch, Jr. Thermal and optical emission and capture rates and cross sections of electrons and holes at imperfection centers in semiconductors from photo and dark junction current and capacitance experiments. *Solid State Electron.*, 13:759, 1970.
- [55] G. P. Li and K. L. Wang. A novel technique for studying electric field effect of carrier emission from a deep level center. *Appl. Phys. Lett.*, 42:838, 1983.
- [56] G. P. Li and K. L. Wang. Detection sensitivity and spatial resolution of reverse-bias pulsed deep-level transient spectroscopy for studying electric field-enhanced carrier emission. *J. Appl. Phys.*, 57:1016, 1985.
- [57] G. Ferenczi, J. Boda, and T. Pavelka. Isothermal frequency scan DLTS. *Phys. Stat. Sol. A*, 94:K119–K124, 1986.
- [58] A. Wessel. Transiente Störstellenspektroskopie an Cu(In,Ga)(S,Se)<sub>2</sub>-Dünnschicht-solarzellen. Diplomarbeit, Universität Oldenburg, Juli 2002.
- [59] S. A. Studenikin, N. Golego, and M. Cocivera. Improved Laplace transform method to determine trap densities from transients: application to ZnO and TiO<sub>2</sub> films. *Semicond. Sci. Tech.*, 13:1383, 1998.
- [60] D. B. Jackson and C. T. Sah. Two deep hole traps in boron-implanted phosphorus-doped silicon. *J. Appl. Phys.*, 58:1270, 1985.
- [61] L. Stolt and K. Bohlin. Deep-level transient spectroscopy measurements using high Schottky barriers. *Solid State Electron.*, 28:1215, 1985.
- [62] F. D. Auret and M. Nel. Detection of minority-carrier defects by deep-level transient spectroscopy using Schottky barrier diodes. *J. Appl. Phys.*, 61:2546, 1987.
- [63] N. Fourches. Deep level transient spectroscopy based on conductance transients. *Appl. Phys. Lett.*, 58:364, 1991.

- [64] A. Broniatowski, A. Blosser, P. C. Srivastava, and J. C. Bourgoin. Transient capacitance measurements on resistive samples. *J. Appl. Phys.*, 54:2907, 1983.
- [65] M. D. Chen, D. V. Lang, W. C. Dautremont-Smith, A. M. Sergent, and J. P. Harbison. Effects of leakage current on deep level transient spectroscopy. *Appl. Phys. Lett.*, 44:790, 1984.
- [66] L. Dobaczewski, P. Kaczor, I. D. Hawkins, and A. R. Peaker. Laplace transform deep-level transient spectroscopic studies of defects in semiconductors. *J. Appl. Phys.*, 76:194, 1994.
- [67] M. Igalson, M. Wimbor, and J. Wennerberg. The change of the electronic properties of CIGS devices induced by damp heat treatment. *Thin Solid Films*, 403/404:302, 2002.
- [68] A. Niemegeers, M. Burgelman, R. Herberholz, U. Rau, D. Hariskos, and H. W. Schock. Model for electronic transport in Cu(In,Ga)Se<sub>2</sub> solar cells. *Prog. Photovolt.*, 6:407, 1998.
- [69] D. V. Lang, H. G. Grimmeiss, E. Meijer, and M. Jaros. Complex nature of gold-related deep levels in silicon. *Phys. Rev. B*, 22:3917, 1980.
- [70] A. Niemegeers and M. Burgelman. Effects of the Au/CdTe back contact on the IV and CV characteristics of Au/CdTe/CdSe/TCO solar cells. *J. Appl. Phys.*, 81:2881, 1997.
- [71] C. Deibel, V. Dyakonov, J. Parisi, J. Palm, S. Zweigart, and F. Karg. Influence of damp heat testing on the electrical characteristics of Cu(In,Ga)(S,Se)<sub>2</sub> solar cells. *Thin Solid Films*, 403/404:325, 2002.
- [72] M. Schmidt, D. Braunger, R. Schäffler, H. W. Schock, and U. Rau. Influence of damp heat on the electrical properties of Cu(In,Ga)Se<sub>2</sub> solar cells. *Thin Solid Films*, 361/362:283, 2000.
- [73] C. Deibel, V. Dyakonov, J. Parisi, J. Palm, S. Zweigart, and F. Karg. Electrical characterization of damp-heat treated Cu(In,Ga)(S,Se)<sub>2</sub> solar cells. In B. McNelis, W. Palz, H. A. Ossenbrink, and P. Helm, editors, *Proceedings of the 17th European Photovoltaic Solar Energy Conference, Munich, Germany*, page 1229, WIP, München, 2002.
- [74] M. Igalson and H. W. Schock. The metastable changes of the trap spectra of CuInSe<sub>2</sub>-based heterojunction photovoltaic devices. *J. Appl. Phys.*, 80:5765, 1996.
- [75] D. J. Chadi and K. J. Chang. Energetics of DX-center formation in GaAs and Al<sub>x</sub>Ga<sub>1-x</sub>As alloys. *Phys. Rev. B*, 39:10063, 1989.
- [76] L. Dobaczewski, P. Kaczor, M. Missous, A. R. Peaker, and Z. R. Zytikiewicz. Structure of the DX state formed by donors in (Al,Ga)As and Ga(As,P). *J. Appl. Phys.*, 78:2468, 1995.
- [77] T. R. Hanak, A. M. Bakry, D. J. Dunlavy, F. Abou-Elfotouh, R. K. Ahrenkiel, and M. L. Timmons. Deep-level transient spectroscopy of AlGaAs and CuInSe<sub>2</sub>. *Sol. Cells*, 27:347, 1989.

- [78] F. A. Abou-Elfotouh, L. L. Kazmerski, A. M. Bakry, and A. Al-Douri. Correlations of single crystal CuInSe<sub>2</sub> surface processing with defect levels and cell performance. In *Proceedings of the 21st IEEE Photovoltaic Specialists Conference, Kissimmee, USA*, page 541, IEEE, New York, 1990.
- [79] F. A. Abou-Elfotouh, H. Moutinho, A. Bakry, T. J. Coutts, and L. L. Kazmerski. Characterization of the defect levels in copper indium diselenide. *Sol. Cells*, 60:151, 1991.
- [80] C. Deibel, A. Wessel, V. Dyakonov, J. Parisi, J. Palm, and F. Karg. Deep levels in stoichiometry-varied Cu(In,Ga)(S,Se)<sub>2</sub> solar cells. *Thin Solid Films*, 2002. In press.
- [81] M. Burgelman, P. Nollet, and S. Degraeve. Modelling polycrystalline semiconductor solar cells. *Thin Solid Films*, 361/362:527, 2000.
- [82] H. Pauwels and G. Vanhoutte. The influence of interface states and energy barriers on the efficiency of heterojunction solar cells. *J. Phys. D: Appl. Phys.*, 11:649, 1978.
- [83] J. Palm. Private Communications, 2002.
- [84] R. Herberholz, T. Walter, C. Müller, T. Friedlmeier, and H. W. Schock. Meyer-Neldel behaviour of deep level parameters in heterojunctions to Cu(In,Ga)(S,Se)<sub>2</sub>. *Appl. Phys. Lett.*, 69:2888, 1996.
- [85] M. Igalson, A. Kubiacyk, and P. Zabierowski. Deep centers and fill factor losses in the CIGS devices. In *Proceedings of the Materials Research Society Symposium, San Francisco, USA*, volume 668, 2001.
- [86] A. Yelon, B. Movaghar, and H. M. Branz. Origin and consequences of the compensation (Meyer-Neldel) law. *Phys. Rev. B*, 46:12244, 1992.
- [87] M. Igalson, A. Kubiacyk, P. Zabierowski, M. Bodegård, and K. Granath. Electrical characterization of ZnO/CdS/Cu(In,Ga)Se<sub>2</sub> devices with controlled sodium content. *Thin Solid Films*, 387:225, 2001.
- [88] A. Broniatowski and J. C. Bourgoin. Transient-capacitance measurement of the grain boundary level in semiconductors. *Phys. Rev. Lett.*, 48:424, 1982.
- [89] R. Scheer, C. Knieper, and L. Stolt. Depth dependent collection function in thin film chalcopyrite solar cells. *Appl. Phys. Lett.*, 67:3007, 1995.
- [90] R. Scheer, M. Wilhelm, and L. Stolt. Temperature dependent electron beam induced current experiments on chalcopyrite thin film solar cells. *Appl. Phys. Lett.*, 70:1011, 1997.
- [91] M. Igalson, M. Bodegård, L. Stolt, and A. Jasenek. The defected layer and the mechanism of the interface-related metastable behaviour of the ZnO/CdS/Cu(In,Ga)Se<sub>2</sub> devices. *Thin Solid Films*, 2002. In press.
- [92] P. Zabierowski and M. Igalson. Thermally assisted tunnelling in Cu(In,Ga)Se<sub>2</sub>-based photovoltaic devices. *Thin Solid Films*, 361/362:268, 2000.

- [93] A. V. Los and M. S. Mazzola. Semiconductor impurity parameter determination from Schottky junction thermal admittance spectroscopy. *J. Appl. Phys.*, 89:3999, 2001.
- [94] D. Cahen and R. Noufi. Surface passivation of polycrystalline, chalcogenide based photovoltaic cells. *Sol. Cells*, 30:53, 1991.
- [95] J.-F. Guillemoles, L. Kronik, D. Cahen, U. Rau, A. Jasenek, and H.-W. Schock. Stability issues of Cu(In,Ga)Se<sub>2</sub>-based solar cells. *J. Phys. Chem. B*, 104:4849, 2000.
- [96] M. Powalla and B. Dimmler. Process development of high performance CIGS modules for mass production. *Thin Solid Films*, 387:251, 2001.
- [97] J. Wennerberg, J. Kessler, M. Bodegård, and L. Stolt. Damp heat testing of high performance CIGS thin film solar cells. In J. Schmid, H. A. Ossenbrink, P. Helm, H. Ehmann, and E. D. Dunlop, editors, *Proceedings of the 2nd World Conference on Photovoltaic Energy Conversion, Luxembourg*, page 116, European Commission, Brussels, 1998.
- [98] G. A. Medvedkin, E. I. Terukov, Y. Hasegawa, K. Hirose, and K. Sato. Microdefects and point defects optically detected in cu(in,ga)se<sub>2</sub> thin film solar cells exposed to the damp and heating. *Sol. Ener. Mat. Sol. Cells*, 2002. In press.
- [99] D. E. Tarrant, A. R. Ramos, D. R. Willett, and R. R. Gay. CuInSe<sub>2</sub> module environmental durability. In *Proceedings of the 21st IEEE Photovoltaic Specialists Conference, Kissimmee, USA*, page 553, 1990.
- [100] J. Wennerberg, J. Kessler, and L. Stolt. Cu(In,Ga)Se<sub>2</sub>-based thin-film photovoltaic modules optimized for long-term performance. *Sol. Ener. Mat. Sol. Cells*, 2002. In press.
- [101] D. V. Lang, J. D. Cohen, and J. P. Harbison. Measurement of the density of gap states in hydrogenated amorphous silicon by space charge spectroscopy. *Phys. Rev. B*, 25:5285, 1982.
- [102] I. Dirnstorfer, D. M. Hofmann, D. Meister, B. K. Meyer, W. Riedl, and F. Karg. Post-growth thermal treatment of CuIn(Ga)Se<sub>2</sub>: Characterization of doping levels in In-rich thin films. *J. Appl. Phys.*, 85:1423, 1999.
- [103] J. D. Cohen and D. V. Lang. Calculation of the dynamic response of Schottky barriers with a continuous distribution of gap states. *Phys. Rev. B*, 25:5321, 1982.
- [104] J. Krauser, T. Riedle, R. Klenk, J. Klaer, M. C. Lux-Steiner, and A. Weidinger. Hydrogen concentration in chalcopyrite thin-film solar cells. *Appl. Phys. A*, 70:617, 2000.



# A List of Investigated Samples

Sample	Number	Remarks
Reference	[923] 8495-2x	Cu/(In+Ga)~0.92
Reference	[982] 9781-0x	Cu/(In+Ga)~0.92
24h DH	[982] 9781-1x	
144h DH	[923] 8495-3x	
294h DH	[923] 8495-0x	
438h DH	[923] 8495-1x	
6h DH after RTP	[982] 9784-1x	
24h DH after RTP	[982] 9781-2x	
24h DH after CdS	[982] 9782-0x	
24h DH after i-ZnO	[982] 9782-2x	
24h boiling H <sub>2</sub> O after RTP	[982] 9783-2x	
30min Oxidation at 200°C after RTP	[982] 9784-2x	
24h Oxidation at 85°C after RTP	[982] 9383-0x	
Schottky Cr/CIGSSe reference	10549-1A	
Schottky Cr/CIGSSe 24h DH	10549-1B	
Schottky Cr/CdS/CIGSSe reference	10548-1A	
Schottky Cr/CdS/CIGSSe 24h DH	10548-1B	
Schottky Cr/CIGSSe Cu-rich	10532-1A	Cu/(In+Ga)~0.97
Schottky Cr/CIGSSe Cu-rich 24h DH	10532-1B	Cu/(In+Ga)~0.97
Na rich	[957] 9346-3x	50% more Na
Na poor	[974] 9533-0x	no Na precursor (more oxygen)
Na poor 24h DH	[974] 9533-1x	
Cu rich	[943] 9233-3x	Cu/(In+Ga)~0.97
Cu rich 264h DH	[943] 9233-1x	
Cu+Na rich	[975] 9640-2x	Cu/(In+Ga)~0.97, 50% more Na
Cu+Na rich 24h DH	[975] 9640-3x	
CVD-ZnO/CdS/Cu(In,Ga)Se <sub>2</sub>	[866] 8047-0x	
CVD-ZnO/ZnSe/Cu(In,Ga)Se <sub>2</sub>	[866] 8051-0x	



## B List of Symbols

Symbol	Description	Unit
$A$	active area of the samples	$\text{m}^2$
$\alpha$	absorption coefficient	$1/\text{m}\sqrt{\text{eV}}$
$C$	capacitance	F
$\Delta C$	amplitude of the capacitance transient	F
$C_p$	capacitance in a parallel configuration	F
$\delta C_p$	change in the capacitance in a parallel configuration	F
$C_s$	capacitance in a serial configuration	F
$\delta C_s$	change in the capacitance in a serial configuration	F
$c_n$	capture rate for electrons	$\text{m}^3/\text{s}$
$c_p$	capture rate for holes	$\text{m}^3/\text{s}$
$d$	layer thickness	m
$E_C$	conduction band minimum	J (eV)
$E_c$	characteristic energy (Meyer-Neldel rule)	J (eV)
$E_g$	energy band gap	J (eV)
$E_V$	valence band maximum	J (eV)
$\Delta E_{PF}$	emission barrier reduction by Poole-Frenkel effect	J (eV)
$\Delta E_\sigma$	energy barrier for carrier capture	J (eV)
$\Delta E_t$	activation energy of a defect state	J (eV)
$e$	elementary charge	C
$e_n$	emission rate for electrons	1/s
$e_p$	emission rate for holes	1/s
$\epsilon_0$	dielectric constant in free space	F/m
$\epsilon_s = \epsilon_r \epsilon_0$	dielectric constant of semiconductor	F/m
$\eta$	power conversion efficiency	
$FF$	fill factor	
$f_t$	occupancy probability of electrons in a trap	
$G$	conductance	S
$G$	Gibbs free energy	J (eV)
$\Delta G$	change in Gibbs free energy	J (eV)
$\Delta H$	enthalpy	J (eV)
$I_{sc}$	short-circuit current	A
$k$	Boltzmann factor	J/K (eV/K)

Symbol	Description	Unit
$\chi$	electron affinity	J (eV)
$\chi_n$	entropy factor	
$\lambda$	intersection point of defect state with Fermi level	m
$\mu_n$	mobility of electrons	cm <sup>2</sup> /Vs
$\mu_p$	mobility of holes	cm <sup>2</sup> /Vs
$N_A - N_D$	net doping density	m <sup>-3</sup>
$N_C$	effective density of states in the conduction band	m <sup>-3</sup>
$N_V$	effective density of states in the valence band	m <sup>-3</sup>
$N_t$	total trap concentration	m <sup>-3</sup>
$n$	concentration of electrons in the conduction band	m <sup>-3</sup>
$n_t$	concentration of trapped electrons	m <sup>-3</sup>
$\nu_0$	attempt-to-escape frequency	Hz
$\nu_{00}$	temperature-independent part of the attempt-to-escape frequency	Hz
$\omega$	frequency of the alternating voltage (AS)	Hz
$\omega_0$	frequency related to $e_t$	Hz
$p$	concentration of holes in the valence band	m <sup>-3</sup>
$p_t$	concentration of trapped holes	m <sup>-3</sup>
$Q$	quality factor, measure for influence of series resistance on DLTS	
$R$	resistance	$\Omega$
$R_s$	series resistance	$\Omega$
$\Delta S$	entropy	J/K (eV/K)
$\sigma_t$	capture cross-section of defect state	m <sup>2</sup>
$T$	absolute temperature	K
$T_c$	characteristic temperature (Meyer-Neldel rule)	K
$t$	time	s
$t_f$	filling pulse width (DLTS)	s
$V$	applied bias	V
$\Delta V$	filling pulse height (DLTS)	V
$V_f$	bias during the filling pulse (DLTS)	V
$V_{oc}$	open-circuit voltage	V
$V_r$	quiescent reverse bias (DLTS)	V
$W$	width of the depletion region	m
$V_{bi}$	built-in potential	V
$\bar{v}_{n,p}$	thermal velocity of electrons/holes	m/s
$Y$	admittance (complex)	S
$Z$	impedance (complex)	$\Omega$

# C Parameters and Results of the Numerical Simulations

## Cu(In,Ga)(S,Se)<sub>2</sub> Solar Cell Parameters

	p-Cu(In,Ga)(S,Se) <sub>2</sub> Absorber	n-CdS Buffer	i-ZnO Window	n-ZnO Window
$d$ [nm]	1000	20	50	500
$\epsilon_r$	10	10	10	10
$\chi$ [eV]	4.5	4.45	4.55	4.55
$E_g$ [eV]	1.1	2.45	3.4	3.4
$\bar{v}_n$ [cm/s]	$10^7$	$10^7$	$10^7$	$10^7$
$\bar{v}_p$ [cm/s]	$10^7$	$10^7$	$10^7$	$10^7$
$\mu_n$ [cm <sup>2</sup> /Vs]	50	50	50	50
$\mu_p$ [cm <sup>2</sup> /Vs]	20	20	20	20
$N_C$ [cm <sup>-3</sup> ]	$2 \times 10^{18}$	$2 \times 10^{18}$	$4 \times 10^{18}$	$4 \times 10^{18}$
$N_V$ [cm <sup>-3</sup> ]	$2 \times 10^{18}$	$1.5 \times 10^{19}$	$9 \times 10^{18}$	$9 \times 10^{18}$
$ N_A - N_D $ [cm <sup>-3</sup> ]	$5.5 \times 10^{15}$	$10^{15}$	$10^{15}$ or $10^{18}$	$10^{20}$
$\alpha$ [1/cm $\sqrt{eV}$ ]	$10^9$	$10^9$	$10^9$	$10^9$

The SCAPS simulation parameters are based on Ref. [68].

## Deep Traps and Interface Defect States

	p-Cu(In,Ga)(S,Se) <sub>2</sub> Absorber	Interface	CdS Buffer	i/n-ZnO Window
Energy Level $\Delta E$ [eV]	0.45	0.55	uniform	midgap
Charge Type	acceptor	neutral	donor	donor
Concentration $N$ [cm <sup>-3</sup> ]	$10^{15}$	$10^{16}$		$10^{17}$
Capture Cross-Section $\sigma$ [eV]	$5 \times 10^{-14}$	$10^{-15}$		$10^{-15}$
Recombination Velocity [cm/s]		$5 \times 10^4$		

The energy levels are given relative to the conduction band.

### Cu(In,Ga)(S,Se)<sub>2</sub> Solar Cells (i-ZnO doping $10^{18}\text{cm}^{-3}$ )

			$V_{oc}$ [mV]	$I_{sc}$ [mA]	$FF$ [%]	$\eta$ [%]	$\Delta E$ [meV]
<b>Reference</b>			<b>573</b>	<b>39.4</b>	<b>72.1</b>	<b>16.3</b>	<b>161</b>
Cu(In,Ga)(S,Se) <sub>2</sub> doping	(1)	$2.5 \times 10^{15}\text{cm}^{-3}$	546	39.6	70.8	15.3	141
acceptor 0.45eV	(2)	$10^{16}\text{cm}^{-3}$	<b>488</b>	36.8	65.0	<b>11.7</b>	182
		$10^{14}\text{cm}^{-3}$	602	39.7	76.2	18.2	158
recombination 0.55eV		$10^{17}\text{cm}^{-3}$	540	38.7	69.2	14.5	161
		$10^{15}\text{cm}^{-3}$	577	39.4	72.6	16.5	161
Cu(In,Ga)(S,Se) <sub>2</sub> /CdS		$5 \times 10^5\text{cm/s}$	565	38.3	71.3	15.5	130
interface	(3)	$5 \times 10^3\text{cm/s}$	577	39.5	72.2	16.5	174
		$5 \times 10^2\text{cm/s}$	577	39.6	72.2	16.5	176
i-ZnO/n-ZnO doping	(4)	$10^{12}/10^{17}\text{cm}^{-3}$	553	39.3	72.7	15.8	214
		$10^{10}/10^{15}\text{cm}^{-3}$	550	39.2	72.7	15.7	219
(1)–(3)			465	37.1	62.9	10.8	191
(1)–(4)			464	36.9	62.1	10.6	341

### Selected Results for Reduction of the Interface Recombination Velocity by One Order of Magnitude

			$V_{oc}$ [mV]	$I_{sc}$ [mA]	$FF$ [%]	$\eta$ [%]	$\Delta E$ [meV]
<b>Reference here:</b>	<b>(3)</b>		<b>577</b>	<b>39.5</b>	<b>72.2</b>	<b>16.5</b>	<b>174</b>
Cu(In,Ga)(S,Se) <sub>2</sub> doping		$2.5 \times 10^{15}\text{cm}^{-3}$	548	40.0	71.2	15.6	147
acceptor 0.45eV		$10^{16}\text{cm}^{-3}$	<b>489</b>	37.0	65.0	<b>11.8</b>	206
recombination 0.55eV		$10^{17}\text{cm}^{-3}$	541	38.9	69.3	14.6	174
i-ZnO/n-ZnO doping		$10^{12}/10^{17}\text{cm}^{-3}$	563	39.3	70.9	15.7	325

## Cu(In,Ga)(S,Se)<sub>2</sub> Solar Cells (i-ZnO doping $10^{15}\text{cm}^{-3}$ )

			$V_{oc}$ [mV]	$I_{sc}$ [mA]	$FF$ [%]	$\eta$ [%]	$\Delta E$ [meV]
<b>Reference</b>			<b>554</b>	<b>39.3</b>	<b>72.7</b>	<b>15.8</b>	<b>212</b>
Cu(In,Ga)(S,Se) <sub>2</sub> doping	(1)	$2.5 \times 10^{15}\text{cm}^{-3}$	540	39.6	70.6	15.1	199
acceptor 0.45eV	(2)	$10^{16}\text{cm}^{-3}$	<b>485</b>	36.8	64.7	<b>11.6</b>	226
		$10^{14}\text{cm}^{-3}$	570	39.7	76.2	17.2	210
recombination 0.55eV		$10^{17}\text{cm}^{-3}$	531	38.6	69.3	16.1	212
		$10^{15}\text{cm}^{-3}$	557	39.4	73.3	17.2	212
Cu(In,Ga)(S,Se) <sub>2</sub> /CdS		$5 \times 10^5\text{cm/s}$	556	38.3	71.6	15.2	152
interface	(3)	$5 \times 10^3\text{cm/s}$	564	39.3	71.3	15.8	<b>310</b>
		$5 \times 10^2\text{cm/s}$	582	39.2	70.4	16.1	<b>389</b>
i-ZnO/n-ZnO doping	(4)	$10^{12}/10^{17}\text{cm}^{-3}$	552	39.3	72.7	15.8	215
		$10^{10}/10^{15}\text{cm}^{-3}$	550	39.2	72.7	15.7	219
(1)–(3)			464	37.0	62.3	10.7	326
(1)–(4)			464	36.9	62.1	10.6	343

### Selected Results for Reduction of the Interface Recombination Velocity by One Order of Magnitude

			$V_{oc}$ [mV]	$I_{sc}$ [mA]	$FF$ [%]	$\eta$ [%]	$\Delta E$ [meV]
<b>Reference here:</b>	<b>(3)</b>		<b>564</b>	<b>39.3</b>	<b>71.3</b>	<b>15.8</b>	<b>310</b>
Cu(In,Ga)(S,Se) <sub>2</sub> doping		$2.5 \times 10^{15}\text{cm}^{-3}$	545	40.0	70.9	15.4	271
acceptor 0.45eV		$10^{16}\text{cm}^{-3}$	<b>487</b>	36.5	63.9	<b>11.4</b>	347
recombination 0.55eV		$10^{17}\text{cm}^{-3}$	536	38.6	68.4	14.2	310
i-ZnO/n-ZnO doping		$10^{12}/10^{17}\text{cm}^{-3}$	563	39.3	70.9	15.7	327





# Lebenslauf

Carsten Deibel

geboren am 11. Februar 1975 in Wuppertal

ledig

## Schulbildung

1981 – 1985 Grundschule Leipziger Straße, Wuppertal

1985 – 1994 Gymnasium St. Anna, Wuppertal

Abitur, Note 2,2 (gut)

## Zivildienst

7/1994 – 9/1995 Betreuung älterer Menschen, Philippuskirche, Wuppertal

## Studium

10/1995 – 9/1997 Physik (Diplom) an der Ruhr-Universität Bochum

9/1997 Vordiplom, Note 2 (gut)

10/1997 – 6/1998 Auslandsstudium an der University of Sussex

6/1998 Certificate of Physics, Note 1 (first grade)

10/1998 – 9/1999 Master an der University of Sussex bei Prof. P. D. Townsend

Thema: *Laser Annealing of Copper and Silver Colloids in Fused Quartz*

1/2000 Master of Philosophy. Dieser Abschluß ist unbenotet.

## Promotion

11/1999 – 12/2002 Promotion an der Universität Oldenburg bei Prof. J. Parisi

Thema: *Defect Spectroscopy on Cu(In,Ga)(S,Se)<sub>2</sub>-based Hetero-junction Solar Cells*

12/2002 Abschluß der Promotion. Note 1 (magna cum laude)



## **Erklärung gemäß §8(2) der Promotionsordnung**

Hiermit erkläre ich, daß ich diese Arbeit selbständig verfaßt und nur die angegebenen Hilfsmittel benutzt habe.

Oldenburg, den 7. November 2002

(Carsten Deibel)

